

Impact of Rotor-Casing Effusion Cooling on Turbine Performance and Operating Point: An Experimental, Computational, and Theoretical Study

Maxwell G. Adams

Department of Engineering Science,
University of Oxford,
Parks Road,
Oxford OX1 3PJ, UK
e-mail: max@maxadams.com

Paolo Adami

Rolls-Royce Deutschland,
Eschenweg 11,
15827 Blankenfelde-Mahlow, Germany
e-mail: paolo.adami2@rolls-royce.com

Matthew Collins

Department of Engineering Science,
University of Oxford,
Parks Road,
Oxford OX1 3PJ, UK
e-mail: matt.collins@oxford-flow.com

Paul F. Beard

Department of Engineering Science,
University of Oxford,
Parks Road,
Oxford OX1 3PJ, UK
e-mail: paul.beard@eng.ox.ac.uk

Kam S. Chana

Department of Engineering Science,
University of Oxford,
Parks Road,
Oxford OX1 3PJ, UK
e-mail: kam.chana@eng.ox.ac.uk

Thomas Povey¹

Department of Engineering Science,
University of Oxford,
Parks Road,
Oxford OX1 3PJ, UK
e-mail: thomas.povey@eng.ox.ac.uk

It is known that a secondary effect of rotor-casing effusion cooling is to modify and potentially spoil the rotor over-tip leakage flow. Studies have shown both positive and negative impacts on high-pressure (HP) stage aerodynamic performance and heat transfer, although there remains no consensus on whether the net effect is beneficial when both aerodynamic and thermal effects are accounted for simultaneously. An effect that has not been extensively discussed in the literature is the change in stage operating point that arises due to mass introduction midway through the machine. This effect complicates the analysis of the true performance impact on a turbine and must be accounted for in an assessment of the overall benefit of such a system. In this paper, we develop a low-order (“mean-line”) analysis in an attempt to bring clarity to this issue. We then present results from experiments conducted in the Oxford Turbine Research Facility, a 1.5-stage transonic rotating facility capable of matching non-dimensional engine conditions. In the experiments, effusion cooling was implemented over a sector of the rotor casing spanning 24 degrees or four rotor-blade pitches. Rotor-exit radial traverse and HP vane loading measurements were conducted locally to the cooled sector. Results are compared to baseline tests conducted without cooling. To assess the degree to which experimental results with only a sector of the annulus cooled would provide an accurate indication of stage operating point changes (when measured local to the annulus) in an annular (engine-like) environment, unsteady Reynolds-averaged Navier–Stokes (URANS) simulations were performed. In particular, simulations of a full annulus with an effusion-cooled sector were compared to a periodic simulation with fully annular effusion cooling. The results—perhaps surprisingly—suggest that a cooled sector is sufficient to infer the changes in an annular system, provided measurements are performed locally to the sector. Experiments conducted with fixed 1.5-stage boundary conditions showed increases in both mid-stage static pressure and stage-exit total pressure with cooling. The mean-line model and URANS predictions were in good agreement with the experimental data and also showed an increase in stage reaction and a reduction in turbine-inlet (mainstream) mass flowrate with cooling. Finally, the URANS predictions were used to show that with cooling, there are changes both locally to the cooled casing (changes to the tip-leakage and secondary flow structures) and globally (changes to the bulk-flow velocity triangles). An absolute stage efficiency benefit of 0.7% was predicted for a coolant-to-mainstream mass flowrate ratio of 2.2%. By running with a number of different boundary conditions, steady RANS simulations were used to estimate the relative contributions to the efficiency improvement due to the changes in operating point and aerodynamics in the blade-tip region. For the present configuration, both changes contribute positively to the improvement in stage efficiency.

[DOI: 10.1115/1.4050019]

Keywords: computational fluid dynamics (CFD), fluid dynamics and heat transfer phenomena in compressor and turbine components of gas turbine engines, heat transfer and film cooling

Introduction

The pursuit of greater turbine entry temperatures has led to increasingly sophisticated cooling schemes that desire to maximize component lifetimes by reducing thermal loads. Casing effusion cooling, as a means to control casing temperatures, has been the

focus of a small number of published research investigations and patents. Chana and Haller [1,2] presented a design methodology for a film cooling system applied to the rotor over-tip casing of the MT1 turbine: a single-stage unshrouded high-pressure (HP) turbine of engine scale. Experimental measurements conducted in a rotating facility at engine-matched non-dimensional conditions showed that with a coolant-to-mainstream mass flowrate ratio of $\dot{m}_c/\dot{m}_1 = 1.85\%$, heat transfer rates were reduced by up to 44% on the rotor over-tip casing near the blade trailing edge (TE).

More recently, Collins et al. [3] reported an experimental and computational study on the same turbine but with a different

¹Corresponding author.

Contributed by the Heat Transfer Division of ASME for publication in the JOURNAL OF TURBOMACHINERY. Manuscript received January 26, 2020; final manuscript received June 24, 2020; published online February 19, 2021. Assoc. Editor: James L. Rutledge.

cooling system design operating at $\dot{m}_c/\dot{m}_1 \approx 1\%$. The authors presented time-resolved casing heat transfer measurements as well as unsteady Reynolds-averaged Navier–Stokes (URANS) predictions with fully mesh-resolved cooling holes. The results revealed a complex interaction between the coolant and tip leakage flows. Furthermore, acoustic effects within the cooling holes, driven by the unsteady potential field of the rotor, were shown to significantly affect unsteady coolant mass fluxes. These acoustic effects were first identified by Collins and Povey [4], who proposed that with correct unsteady design, systems could be designed to operate without ingestion at significantly lower coolant pressures than a steady-state analysis would suggest was possible. Overall, the limited body of open literature suggests that effusion cooling can be effective in cooling the rotor casing at moderate coolant mass flowrates.

Other investigations have suggested that such a system may not only reduce casing heat transfer but also increase rotor efficiency. Mischo et al. [5] reported a computational study, in which coolant was injected from the rotor over-tip casing via a single row of circumferentially distributed holes. An immersed boundary method was used to model the discrete cooling holes, with time-dependent source terms imposed at nodes near the solid casing according to an empirical model coupled with the predicted freestream flow. A reduction in tip leakage mass flowrate of approximately 11% was predicted with $\dot{m}_c/\dot{m}_1 = 0.7\%$ injected at approximately 30% of the blade axial chord. This was attributed to increased blockage and displacement of the tip leakage flow. In a related experimental study by Behr et al. [6], time-resolved area traverse measurements were conducted in a 1.5-stage rotating facility, showing an increase in stage isentropic efficiency of 0.55% for the same cooling configuration. The size and turbulence intensity of the tip leakage vortex (TLV) and upper passage vortex (PV) were also reduced. Other cooling configurations were tested, for which results were less positive, however. With \dot{m}_c/\dot{m}_1 increased to 1.0%, the efficiency benefit reduced to 0.41%, which the authors attributed to reduced rotor torque due to the negative tangential momentum of the injected coolant. In the second case, with coolant injection delayed from 30% to 50% axial chord, efficiency decreased with respect to the uncooled case for both coolant mass flowrates, reportedly because the delayed effect on secondary flow suppression was insufficient to outweigh the reduction in rotor torque. It is noted that in the analysis of Behr et al., the efficiency decrease was attributed, at least in part, to changes in rotor torque. Since efficiency could, in principle, increase while rotor torque decreases, another possible interpretation of the efficiency change might be that it was related to changes in the degree to which the expansion was ideal. That is, the mechanism may be more ambiguous than suggested.

Most published studies on the impact of effusion cooling on stage efficiency focus on changes to secondary flow losses in the rotor tip region when coolant is injected. The studies do not, however, consider the changes in stage operating point that arise due to mass introduction midway through the machine. Changes to the stage operating point can affect loss and efficiency through additional means, such as mismatching of blade rows, while also affecting other important performance metrics, such as turbine power output. The computational studies reviewed above modeled only the rotor domain and not the neighboring blade row(s); boundary conditions were set such that any blade row mismatching effects could not be captured. This paper seeks to clarify the mechanism by which coolant mass introduction affects the turbine operating point. It will be demonstrated that once quantified, the shift in operating point can be accounted for, such that the interpretation of efficiency changes due to coolant introduction can be corrected.

The structure of this paper is as follows. First, a mean-line model is developed and used to clarify the mechanism by which mass introduction midway through the turbine affects the HP stage operating point in the absence of complicating phenomena such as tip leakage flow spoiling. The experimental setup is then described, and experimental results are presented for first vane loading distributions and rotor-exit radial traverse measurements. The

computational fluid dynamics (CFD) setup is then described, in which the full 1.5-stage domain is modeled in order to capture changes to the turbine operating point. The impact of cooling only a sector of the rotor casing is assessed using full-annulus CFD predictions in order to evaluate the extent to which the experimental configuration reflects a fully periodic environment. Finally, the CFD model is used to predict the change in HP stage efficiency due to coolant introduction and to estimate the relative contributions due to the changes in operating point and tip leakage flow structure (by altering the boundary conditions).

Mean-Line Model

Given inlet boundary conditions of total pressure, p_{01} , and total temperature, T_{01} , and an exit boundary condition of static pressure, p_4 , a mean-line model of a 1.5-stage turbine can be constructed. If the capacity characteristics for each blade row are known, the continuity equations can be solved iteratively for the mainstream mass flowrate at turbine inlet, \dot{m}_1 , and inter-row static pressures at HP vane and rotor exit, p_2 and p_3 , respectively. (It will be shown later that when a nonzero coolant mass flow rate, \dot{m}_c , is introduced to the model, \dot{m}_1 depends on \dot{m}_c .) In the present model, the capacity characteristics for each blade row are based on Reynolds-averaged Navier–Stokes (RANS) predictions. To solve the continuity equations, the inter-row stagnation conditions, $p_{02,rel}$ and p_{03} , are calculated using velocity triangles and a total pressure loss estimation method proposed by Kacker and Okapuu [7] and improved by Benner et al. [8]. Further details of the mean-line calculation are given in the Appendix.

We now introduce two simplified models, in which the coolant injection process is spatially confined, in order to understand the sensitivity of the turbine operating point to \dot{m}_c . In both models, coolant is introduced at discrete stations upstream (\dot{m}_{c2} at Station 2) and downstream (\dot{m}_{c3} at Station 3) of the rotor as illustrated schematically in Fig. 1. In experiments (described later), coolant was injected from an array of casing effusion cooling holes, which extended from just upstream to just downstream of the rotor tip extents. To represent this in the simplified model, the coolant mass flow was arbitrarily split between the two injection points at Stations 2 and 3. In the low-order model, Station 2 is injection before any rotor turning has occurred, and Station 3 is injection

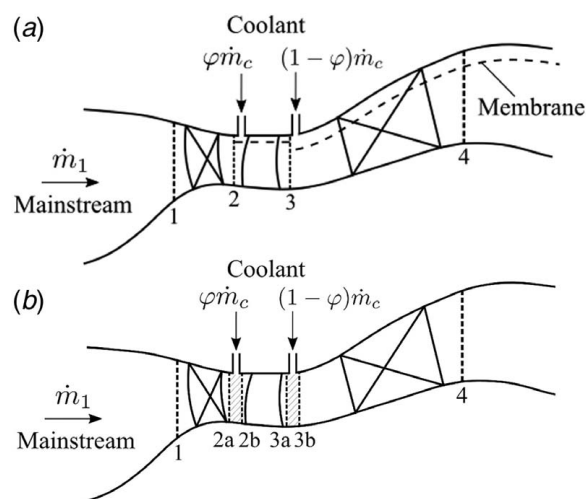


Fig. 1 Illustrations of two conceptual mean-line models featuring coolant injection: (a) the membrane model with no coolant-mainstream mixing, and (b) the mixed-out model with instantaneous coolant-mainstream mixing. The schematic diagram of the turbine geometry corresponds to the 1.5-stage turbine used in experiments.

after rotor turning is complete. We define a coolant mass fraction, φ , as the fraction of the total coolant mass injected at Station 2, before rotor turning. In the low-order model, this value is set to the mass fraction delivered before 50% of flow turning in the experiment (and fully featured CFD). For completeness

$$\varphi = \dot{m}_{c2} / \dot{m}_c \quad (1)$$

where $\dot{m}_c = \dot{m}_{c2} + \dot{m}_{c3}$.

The axial position, x_φ , at which 50% of the flow turning occurs in the rotor was predicted via three-dimensional (3D) URANS simulation of the 1.5-stage turbine without cooling (the baseline case). Figure 2 shows the predicted mass-averaged tangential velocity, \bar{v}_θ , along the machine axis, x . The point of 50% rotor turning, x_φ , is indicated at 70.9% of the rotor blade tip axial chord, C_{ax}^{tip} . Based on the experimental configuration (described later), the leading six rows of casing effusion cooling holes are located upstream of this position. Summing the measured coolant mass flowrates delivered from these rows leads to a mass split of $\varphi \approx 65\%$.

Two variations of the model are used to treat the coolant-mainstream interaction. In the first model, no mixing occurs between the coolant and mainstream flows. Coolant introduction changes the area that the mainstream flow can occupy, as if via a flexible impermeable membrane (same static pressure on either side of the membrane for all x) separating the two streams. We therefore refer to this model as the membrane model. It is noteworthy that the coolant is turned by the rotor and thus has the opportunity to exchange work. The second mean-line model, which we refer to as the mixed-out model, represents the extreme alternative to the membrane model: the coolant and mainstream mix instantaneously and completely (at constant static pressure) at the points of coolant injection. In this case, the mainstream flow mixes with the coolant injected at Station 2 before passing through the rotor, so that the mixed-out stream (total mass flowrate $\dot{m}_1 + \varphi\dot{m}_c$) has the opportunity to perform work on the rotor (as is also true for the membrane model). The mixed-out flow then mixes with the coolant injected at Station 3. At Stations 2 and 3, mixing is assumed to be adiabatic and the total pressure loss is calculated using the Hartsel model [9] (further details are given later).

In both models, the coolant total temperatures at both points of injection were set to $T_{0c} = 290$ K, the nominal coolant supply total temperature in experiments (discussed later). At each iteration in the calculation of \dot{m}_1 , p_2 , and p_3 (see Eqs. (A1)–(A3) in Appendix), the coolant total pressures at the points of injection, p_{0c2} and p_{0c3} , were calculated using the compressible mass flowrate equation. At Station 2, for example, p_{0c2} was calculated using

$$\dot{m}_{c2} = \frac{A_{c2,eff} p_{0c2}}{\sqrt{T_{0c}}} \left(\frac{p_{0c2}}{p_2} \right)^{-\frac{\gamma+1}{2\gamma}} \left\{ \frac{2\gamma}{R(\gamma-1)} \left[\left(\frac{p_{0c2}}{p_2} \right)^{\frac{\gamma-1}{\gamma}} - 1 \right] \right\}^{1/2} \quad (2)$$

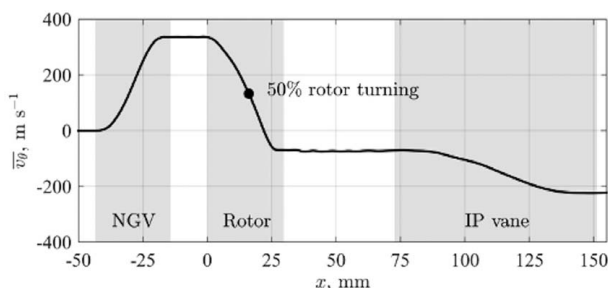


Fig. 2 Predicted mass-averaged tangential velocity plotted along the machine axial coordinate. The axial extents covered by the blade rows are indicated, as is the point of 50% flow turning by the rotor. Data presented are obtained from a time-averaged URANS prediction without cooling.

where $A_{c2,eff}$ is the sum of the experimentally measured effective areas of all rows of cooling holes upstream of x_φ . To calculate p_{0c3} , a modified Eq. (2) was used, in which quantities at Station 2 are replaced with those at station 3. The calculations of p_{0c2} and p_{0c3} are themselves iterative within each outer iteration of the main solver (which solves for \dot{m}_1 , p_2 , and p_3).

Equation (2) and its counterpart for \dot{m}_{c3} assume that each of the two coolant streams is injected to a (different) single, constant static pressure. In experiments (discussed later), however, there were nine rows of cooling holes on the casing, which exit to nine different temporally varying static pressures. Therefore, the approach employed in the model is a simplified representation of the experiment. The approach allows a simple means of calculating the coolant total pressures that would have been required to deliver the prescribed coolant mass flowrates at the correct total temperatures, had the coolant been injected at two discrete stations before and after the rotor (as is the situation in the model).

In the mixed-out model, the mixed-out total temperatures immediately after coolant injection, T_{02b} and T_{03b} , are calculated at each iteration in the calculation of \dot{m}_1 , p_2 , and p_3 using the adiabatic energy equation applied to the control volumes (CV) at Stations 2 and 3—see Fig. 1(b). The HP vane is assumed adiabatic ($T_{02a} = T_{01}$), and there is no coolant flow introduction in the vane ($\dot{m}_{2a} = \dot{m}_1$). The coolant mass flow rates, \dot{m}_{c2} and \dot{m}_{c3} , and total temperature, T_{0c} , are inputs to the model and so T_{02b} can be calculated straightforwardly. To calculate T_{03a} , the rotor isentropic power and an estimated rotor efficiency (see the Appendix) are used.

The mixed-out total pressures p_{02b} and p_{03b} are calculated using the Hartsel mixing total pressure loss model [9] applied to the same CVs as discussed earlier. At each CV, the Hartsel mixing calculation depends on the stagnation conditions of the coolant and mainstream flows entering the CV, the mainstream Mach number at the inlet to the CV, and a coolant compound injection angle. The injected coolant streams have total pressures calculated using the same method as in the membrane model and equal total temperatures (at $T_{0c} = 290$ K). Compound injection angles at Stations 2 and 3 are based on the actual injection angles of the cooling holes in the experimental hardware (discussed later) upstream and downstream of x_φ , respectively, weighted by their measured coolant mass flowrates.

Using the models outlined previously, mean-line calculations can be repeated at various coolant mass flowrates, turbine boundary conditions (such as the 1.5-stage pressure ratio, p_4/p_{01}), and other turbine operating parameters (such as shaft speed), in order to predict performance trends. In the mean-line analysis presented in this paper, however, p_4/p_{01} and shaft speed are both fixed.

Mean-Line Model Results. This section uses the mean-line model to clarify the mechanism by which coolant introduction midway through the turbine affects the turbine operating point. Figure 3 plots inter-row static pressures, mass flowrates, Mach numbers, flow angles, blade row pressure ratios, stage reaction, stage loading coefficient, and power output, for both the membrane and mixed-out models, as functions of \dot{m}_c from 0 to 4% of the nominal mainstream mass flowrate without cooling, \dot{m}_{1N} , which covers the experimental range (discussed later). For both models, trends are plotted for the mass mean of the coolant and mainstream. For the mixed-out model, relative quantities at Stations 2 and 3 are plotted after and before coolant-mainstream mixing (i.e., at Stations 2b and 3a), respectively.

Comparing results from the two mean-line models, the predicted changes with increasing \dot{m}_c generally agree in trend, although there are differences in magnitude. In both models, coolant introduction at the exit of the HP vane (\dot{m}_{c2} at Station 2) and rotor (\dot{m}_{c3} at Station 3) causes p_2 and p_3 to increase, as shown in Fig. 3(a). Because p_{01} is fixed, and for both models, the change in HP vane total pressure loss is small (below 0.1% points) for all \dot{m}_c considered, the HP vane-exit Mach number, M_2 , decreases with increasing \dot{m}_c primarily as a result of the p_2 increase—see Fig. 3(b). In the

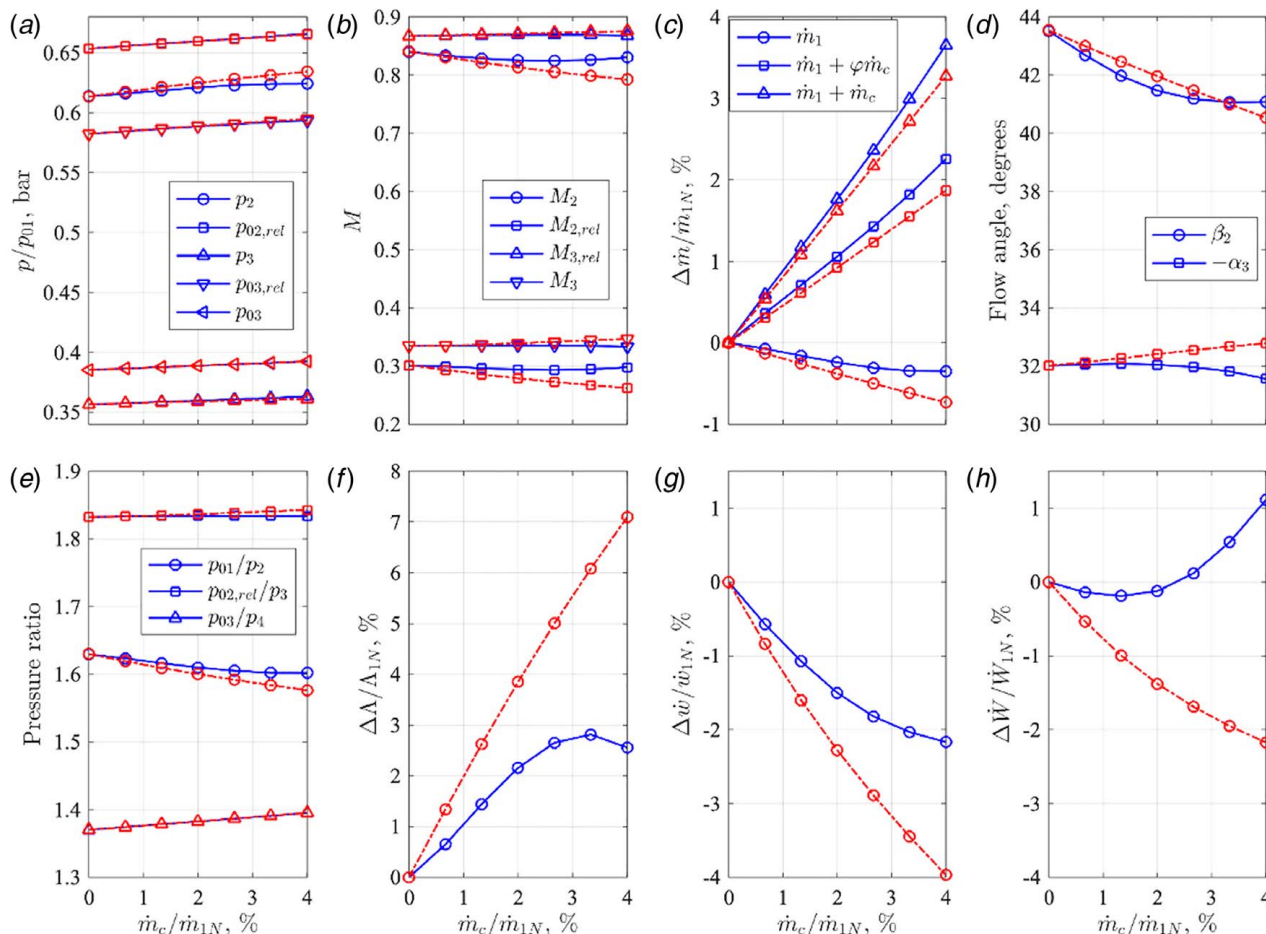


Fig. 3 Predicted trends with varying \dot{m}_c , obtained from the two mean-line models. Solid lines = membrane model; dash-dotted lines = mixed-out model. (a) Inter-row pressures normalized by turbine-inlet total pressure, (b) inter-row Mach numbers, (c) changes in mass flowrates at turbine inlet (\dot{m}_1), rotor inlet ($\dot{m}_1 + \phi\dot{m}_c$), and IP vane inlet ($\dot{m}_1 + \dot{m}_c$) as percentages of the nominal turbine-inlet mass flowrate without cooling (\dot{m}_{1N}), (d) relative yaw angle at rotor inlet and (negative) absolute yaw angle at rotor exit, (e) blade row pressure ratios, (f) normalized stage reaction, (g) normalized mass-mean specific power output, and (h) normalized absolute power output. For the mixed-out model, relative quantities at Stations 2 and 3 are plotted after and before coolant-mainstream mixing (i.e., at Stations 2b and 3a), respectively.

mixed-out model, the Mach number after coolant-mainstream mixing, M_{2b} , decreases at a greater rate than M_2 in the membrane model, partially due to the greater increase in p_2 and partially due to the additional total pressure loss due to mixing (calculated using the Hartsel model).

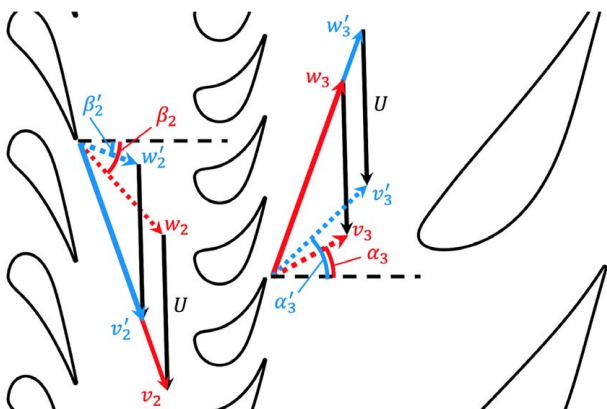


Fig. 4 Velocity triangles at HP vane and rotor exit with and without cooling (not to scale). Prime (') signifies "with cooling." Dashed black lines indicate the axial direction of the machine.

Because T_{01} and the HP-vane capacity characteristic, $\Gamma_1(p_2/p_{01})$, are fixed in both models, the p_2 increase causes \dot{m}_1 to decrease, as shown in Fig. 3(c). Despite the \dot{m}_1 decrease, the mass flowrates through the rotor ($\dot{m}_1 + \phi\dot{m}_c$) and IP vane ($\dot{m}_1 + \dot{m}_c$) both increase as \dot{m}_c increases, due to the lower density of the coolant (mass flowrate is inversely proportional to the square root of total temperature), which accounts for an increasing fraction of the total mass flow through each of these blade rows.

As p_2 rises with increases \dot{m}_c , the absolute velocity at HP vane exit, v_2 , decreases, reducing the rotor-relative velocity, w_2 . As illustrated by the HP vane-exit velocity triangles shown in Fig. 4, this causes a decrease in relative yaw angle at rotor inlet, $\alpha_{2,rel}$, and therefore a decrease in rotor incidence angle. The prediction of this result is shown in Fig. 3(d). In the mixed-out model, the rate of decrease in relative yaw angle after coolant-mainstream mixing, $\alpha_{2b,rel}$, is enhanced due to the lower temperature of the coolant gas.

Figures 3(a) and 3(c) also show predicted changes in relative total pressure, $p_{02,rel}$, and relative Mach number, $M_{2,rel}$, respectively, at rotor inlet due to coolant introduction. In the membrane model, because M_2 decreases and T_{02} is unchanged, T_2 increases. As w_2 decreases, then, the relative Mach number at rotor inlet, given by

$$M_{2,rel} = \frac{w_2}{\sqrt{\gamma RT_2}} \quad (3)$$

also decreases. The trends of p_2 increase and $M_{2,rel}$ decrease are such that the rotor-relative total pressure

$$p_{02,rel} = p_2 \left(1 + \frac{\gamma-1}{2} M_{2,rel}^2 \right)^{\gamma/(\gamma-1)} \quad (4)$$

increases. The mixed-out model predicts a similar trend, but with the rate of decrease in relative Mach number after coolant-mainstream mixing, $M_{2b,rel}$, enhanced, partially due to the additional Hartsel mixing loss and partially due to the reduced mixed-out static temperature.

The changes to the flow at the rotor inlet, as well as the additional coolant introduction at station 3, affect the flow at the rotor exit. In the membrane model, as \dot{m}_c increases, changes in relative total pressure loss across the rotor (those predicted due to off-design incidence angles and Mach numbers using the estimation methods described in Refs. [7] and [8]) are small (less than 0.4% points) for all \dot{m}_c considered, so the relative total pressure at rotor exit, $p_{03,rel}$, increases at a rate close to that of $p_{02,rel}$. While coolant injection at station 3 causes p_3 to increase, $p_{03,rel}$ increases slightly more rapidly than p_3 and so $p_{03,rel}/p_3$ increases slightly. As a result, the relative Mach number at rotor exit, given by

$$M_{3,rel} = \left\{ \frac{2}{\gamma-1} \left[\left(\frac{p_{03,rel}}{p_3} \right)^{\frac{\gamma-1}{\gamma}} - 1 \right] \right\}^{1/2} \quad (5)$$

also increases slightly—see Fig. 3(b). In the mixed-out model, the trend of relative Mach number at rotor exit before coolant-mainstream mixing, $M_{3a,rel}$, virtually overlays with that of $M_{3,rel}$ in the membrane model.

For both models, the predicted change in the local speed of sound, $a_3 = \sqrt{\gamma R T_3}$, is small (less than 0.2%) for all \dot{m}_c considered. As a result, the relative velocity at rotor exit, $w_3 = M_{3,rel} a_3$, increases with $M_{3,rel}$. Because both models assume the flow follows the mean blade angle at rotor exit (i.e., the relative yaw angle at rotor exit, α_3 , rel , is fixed), and because the rotor blade speed, U , is fixed, the (negative) absolute yaw angle at rotor exit, α_3 , increases in magnitude. This is illustrated by the rotor-exit velocity triangles shown in Fig. 4 and is predicted by both models—see Fig. 3(d). It is noteworthy that the increases in α_3 are small (less than 1 deg) over the range of \dot{m}_c considered, and that the membrane model in fact predicts a small decrease in α_3 for \dot{m}_c/\dot{m}_{1N} greater than approximately 2%. This results from the gradual reduction in the rate of increase of p_2 with increasing \dot{m}_c observed in Fig. 3(a).

The rotor-exit velocity triangles (see Fig. 4) show that as w_3 increases, the absolute velocity at rotor exit, v_3 , increases also. Recalling that the changes in α_3 are small, it follows that the absolute Mach number, $M_3 = v_3/a_3$, increases. The increases in M_3 and, moreover, p_3 cause the absolute total pressure at rotor exit, given by

$$p_{03} = p_3 \left(1 + \frac{\gamma-1}{2} M_3^2 \right)^{\gamma/(\gamma-1)} \quad (6)$$

to increase. Predictions of these results are shown in Figs. 3(a) and 3(b). It is noteworthy that the p_{03} increase arises not due to a reduction in losses, which in fact increase very slightly due to the off-design rotor incidence angle (and outweigh the loss reductions in the HP vane due to the reduction in exit Mach number), but rather due directly to the changes to the velocity triangles at HP vane and rotor exit with coolant introduction.

Figure 3(e) shows predicted pressure ratios (upstream total to downstream static) across each blade row. As \dot{m}_c increases, the HP vane pressure ratio decreases while both the rotor and intermediate-pressure (IP) vane pressure ratios increase. Since the capacity characteristics for each blade row are fixed in both models, these trends correspond directly to the changes in mass flow through each row.

The changes to the velocity triangles cause changes in the HP stage reaction

$$\Lambda = \frac{p_2 - p_3}{p_1 - p_3} \quad (7)$$

Figure 3(f) shows the predicted stage reaction as a function of \dot{m}_c/\dot{m}_{1N} . Both models show an increase in reaction for \dot{m}_c/\dot{m}_{1N} below approximately 3.5%. For all \dot{m}_c considered, the increase in reaction is greater in the mixed-out model than in the membrane model. This is predominantly due to the greater rate of increase in p_2 with increasing \dot{m}_c —see Fig. 3(a). For \dot{m}_c/\dot{m}_{1N} greater than approximately 3.5%, the membrane model predicts a decrease in reaction because p_2 starts to decrease. Nevertheless, the predicted reaction is greater with cooling than without, for all \dot{m}_c considered, which indicates that an effect of mass introduction midway through the machine is to increase the proportion of the stage expansion that occurs in the rotor.

The turbine specific power output is affected by changes in flow turning in the rotor

$$\dot{w} = U(v_{\theta 2} - v_{\theta 3}) \quad (8)$$

where $v_{\theta 2} = v_2 \sin \alpha_2$ and $v_{\theta 3} = v_3 \sin \alpha_3$ are the tangential velocities at rotor inlet and exit. Note that for the mixed-out model, the tangential velocities are taken after coolant-mainstream mixing at Station 2 and before coolant-mainstream mixing at Station 3. Since U is fixed in both models, changes in \dot{w} are equivalent to changes in stage loading coefficient. The preceding analysis showed that for both models, v_2 decreases with increasing \dot{m}_c . Since α_2 is fixed in the model (i.e., flow angle at HP vane exit is assumed unchanged with coolant introduction), $v_{\theta 2}$ decreases also. Both v_3 and absolute angle, $|\alpha_3|$, increase with coolant introduction for the mixed-out model, leading to increased $v_{\theta 3}$. In the membrane model, v_3 and α_3 change little with coolant introduction. Because for both models the decrease in $v_{\theta 2}$ is greater than the increase in $v_{\theta 3}$, the flow turning ($v_{\theta 2} - v_{\theta 3}$) decreases and hence the specific power output decreases.

Figure 3(g) presents predicted changes in mass-mean specific power output for the two models. The membrane model predicts that mass-mean \dot{w} decreases with increasing \dot{m}_c . For all \dot{m}_c considered, \dot{w} was predicted to be lower for the coolant stream than for mainstream (not shown). This result is as expected, given that the rotor incidence angles and Mach numbers for the coolant stream are more severely off design for the coolant stream than for the mainstream: the turning is lower, and the loss correlations give higher loss for the coolant stream.

In the mixed-out model, mass-mean \dot{w} again decreases with increasing \dot{m}_c , although the rate of decrease is greater than in the membrane model. This is predominantly because the tangential velocity after coolant-mainstream mixing at Station 2 is reduced due to the lower temperature of the coolant gas.

The turbine absolute power output is affected not only by changes in flow turning, but also by changes in mass flowrate through the rotor. Figure 3(h) presents predicted changes in absolute power output for the two models. The absolute power output of the mainstream flow (not shown) decreases more rapidly than the specific power, as a result of the decrease in mainstream mass flowrate through the rotor, \dot{m}_1 —see Fig. 3(c). However, the total power output due to both the coolant and mainstream flows decreases slightly for $\dot{m}_c/\dot{m}_{1N} < 1.5\%$ and then increases for greater \dot{m}_c/\dot{m}_{1N} . This is due to the fact that at low \dot{m}_c , the trend is influenced by the mainstream (for which the power output is decreasing because \dot{m}_1 and the mainstream specific power output are decreasing), while as \dot{m}_c increases, the trend is influenced to an increasing degree by the coolant stream (for which the power output is increasing because \dot{m}_c and the coolant specific power output are increasing). Note that the coolant specific power output increases with increasing \dot{m}_c because the coolant incidence angle and Mach number at rotor inlet tend toward their design values, thus reducing losses (as modeled by the simple correlations) and increasing flow

turning in the rotor. In the mixed-out model, the absolute power, \dot{w} , decreases less rapidly than \dot{w} because the rotor mass flowrate ($\dot{m}_1 + \dot{q}\dot{m}_c$) increases with increasing \dot{m}_c .

Overall, the results of the mean-line models suggest that for fixed 1.5-stage pressure ratio, the introduction of representative (of proposed effusion cooling systems) coolant mass flowrates midway through the turbine significantly affect the stage operating point. In particular, the HP vane (turbine stage-inlet) mass flow decreases, while the overall rotor mass flow increases; the HP stage reaction increases; and the absolute power output changes (increases for membrane model but decreases for mixed-out model). We will refer to these changes as global effects of cooling, in that they result from changes to the bulk-flow velocity triangles rather than local effects to the tip leakage and secondary flow structures (not included in the simple mean-line models). Both global and local effects can be expected to affect losses. Therefore, when comparing efficiencies with and without cooling, the relative benefits/penalties due to the global/local effects should be considered. The mean-line model is only suitable for analyzing global effects, as in the low-order model, complex interactions and secondary flows are not included.

We conclude this section with a summary table of mean-line model predictions for later comparison to the experimental measurements and CFD predictions. Table 1 lists the predicted changes in selected parameters for $\dot{m}_c/\dot{m}_{1N} = 3.39\%$ (Case C, introduced later) with respect to the uncooled case. Results are shown for both models. For the membrane model, values are listed for the mainstream flow alone and also for the mass-mean flow (coolant plus mainstream), except for \dot{w} , where the total power output due to both streams is reported.

Experimental Setup

We now turn to experimental validation of the key predictions of the mean-line models, in particular the predicted static-pressure rise at rotor inlet with cooling, and the predicted total pressure rise at rotor exit with cooling.

Experimental Facility. The Oxford Turbine Research Facility (OTRF) is a short-duration wind tunnel capable of matching engine conditions of Mach number, Reynolds number, turbulence intensity, and gas-to-wall temperature ratio.

Prior to a run, the test section is evacuated (approximately 10 mbar) and the rotor is spun to the design speed. Test gas is pre-conditioned in a piston tube, ahead of a light free piston. High-pressure air is then injected behind the piston, driving it down the tube and causing approximately isentropic compression of the test

Table 2 LEMCOTEC turbine operating conditions in the OTRF

Parameter	Nominal value
Re_{HPV}	2.13×10^6
M_2	0.956
$\Gamma = \dot{m}\sqrt{T_{01}}/p_{01}$	$5.90 \times 10^{-4} \text{ kg s}^{-1} \text{ K}^{1/2} \text{ Pa}^{-1}$
$N/\sqrt{T_{01}}$	385 rpm $\text{K}^{-1/2}$
p_{01}	8.5 bar
T_{01}	475 K
p_{01}/p_4	3.57
T_{01}/T_w	1.64

gas. A fast-acting plug valve is activated when the design turbine-inlet conditions are reached, allowing the test gas to flow through the working section. The turbine pressure ratio is set using an adjustable-area second throat (normally choked) downstream of the turbine. Downstream of the second throat, the test gas passes through an aerodynamic turbobrake (acting as a compressor) connected to the rotor shaft. The power of the turbobrake is set to maintain a constant rotor speed during the run. Steady conditions are typically achieved for approximately 400 ms. Further details of the facility operation are given by Hilditch et al. [10].

For the present investigation, the facility operated with the low-emissions core engine technologies (LEMCOTEC) turbine, a 1.5-stage research turbine designed by Rolls-Royce and GKN to represent modern engine architectures. The design and commissioning of the turbine is reported by Beard et al. [11]. The design operating conditions of the LEMCOTEC turbine in the OTRF are presented in Table 2.

Cooling Module. In order to reduce the cost and complexity of the experimental hardware, casing effusion cooling was employed only over a 24-deg sector of the rotor over-tip casing, rather than the full casing, using a modular cassette installed in the working section. The cooled sector covered four rotor blade pitches or approximately 2.7 HP vane pitches. A computer-aided design (CAD) model of the cooling module is shown in Fig. 5.

The cooling scheme features nine rows of cylindrical cooling holes 0.50 mm in diameter. Each row lies on an axial plane between -36% and 112% of axial chord at blade tip ($C_{ax}^{tip} = 22.8 \text{ mm}$) with uniform hole spacing in the circumferential direction. The orientation of each hole is defined by two angles: a compound inclination angle and a yaw angle. The compound inclination angle is defined as the angle between the hole axis and the

Table 1 Summary of mean-line model predictions with $p_4/p_{01} = 0.28$ and $\dot{m}_c/\dot{m}_{1N} = 3.39\%$ (Case C)

Parameter	Membrane model		Mixed-out model
	Mainstream	Mass-avg. (or sum*)	
\dot{m}_1		−0.35%	−0.65%
p_2		+1.69%	+3.05%
$p_{02,rel}$	+1.18%	+1.60%	+1.57%
$ \alpha_{2,rel} $	−1.44 deg	−2.45 deg	−4.95 deg
p_3		+1.53%	+1.26%
p_{03}	+1.50%	+1.54%	+1.47%
$ \alpha_3 $	+0.01 deg	+0.22 deg	+0.60 deg
\dot{w}	−1.39%	−2.04%	−3.83%
\dot{W}	−1.73%	+0.59%*	−2.34%

Note: For the membrane model, quantities are listed for the mainstream and the mass-average of the mainstream and coolant stream (except for total power output, \dot{W} , where the sum due to both streams is listed rather than the mass-average). For the mixed-out model, relative quantities at stations 2 and 3 are listed after and before coolant-mainstream mixing (i.e., at stations 2b and 3a), respectively.

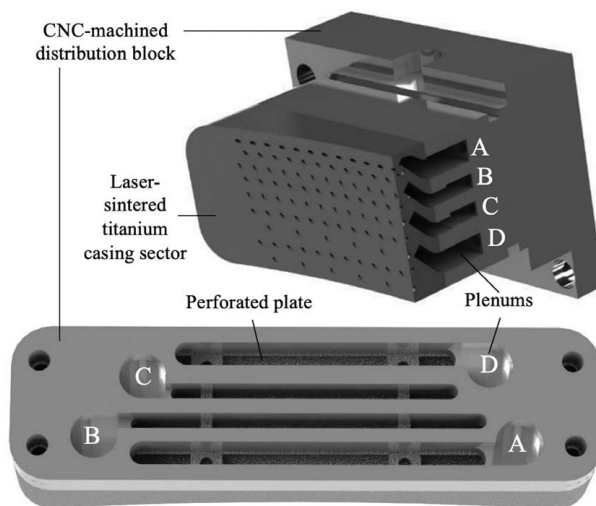


Fig. 5 CAD model of the experimental cooling module

casing surface (i.e., the lay angle of the holes) and was 20 deg for all holes. The yaw angle is defined as the angle between the projections (onto the casing) of the hole axis and the machine axis and was identical for each hole in a given row.

The coolant feed design is based on a design reported by Collins et al. [3]. Each row of cooling holes is supplied by one of four plenums housed within the cooling module. To reduce system transients, the plenum volumes were minimized during the design. The design features a titanium laser-sintered casing sector featuring the cooling holes, which mounts on an aluminum distribution block, machined via computer numerical control (CNC), housing the four plenums within the cassette. To achieve uniform pressure within each plenum, a perforated plate is mounted between the two parts. The titanium part was electrical discharge machining (EDM) wire-cut around its rounded rectangular perimeter in order to minimize clearance when installed in the cassette. The three parts were bonded together with epoxy resin backed by screws. A nitrile O-ring around the module seals the working section from the atmosphere. During uncooled tests, the cooling module was replaced with a solid Perspex block machined to sit flush with the casing. The change in casing endwall loss due to the difference in surface roughness between the titanium and Perspex casing modules are expected to be negligible in comparison with the change caused by cooling introduction.

Coolant Supply and Mass Flow Metering System. Figure 6 shows a schematic diagram of the coolant supply system. During experiments, the mass flowrates to each plenum were individually set using four calibrated choked orifices fed from a common supply manifold. Coolant air was supplied to the manifold from a reservoir at ambient temperature (approximately 290 K) and a pre-set pressure chosen to provide the desired overall coolant mass flowrate, \dot{m}_c . Coolant flow was controlled by a solenoid ball valve upstream of the individual plenum valves. This main valve was opened at the start of each test (using a programmable logic controller triggered on opening of the valves supplying the gas behind the main piston) and closed at the end of each test (triggered by an automatic timer). A steady supply of coolant was maintained throughout each test.

The coolant pressure was measured in the supply manifold and in each of the four plenums using diaphragm-based Sensor Technics CTE 8000 series transducers with nominal uncertainty of $\pm 0.1\%$. The coolant temperature was measured in each plenum using k -type 25 μm bare bead thermocouples.

The coolant mass flowrate through each plenum was calculated using

$$\dot{m}_{ci}(p_{0cm}/p_{ci}) = \frac{p_{0cm}}{\sqrt{T_{0cm}}} \Gamma_{feed,i}(p_{0cm}/p_{ci}) \quad (9)$$

where $\Gamma_{feed,i}(p_{0cm}/p_{ci})$ is the flow capacity characteristic of the plenum feed orifices, p_{0cm} and T_{0cm} are the coolant stagnation conditions within the supply manifold, and $p_{ci} \approx p_{0ci}$ is the pressure within the plenum (by careful design, dynamic pressure is negligible). Through a series of blowdown tests (conducted in a separate facility) exhausting to the atmosphere, the flow capacity characteristics of each orifice were measured over the full range of pressure ratios experienced during OTRF testing. The sensitivity of $\Gamma_{feed,i}(p_{0cm}/p_{ci})$ to the Reynolds number changes and coolant gas properties was not accounted for, as the correction factor was estimated to be small in comparison with the overall uncertainty in the mass flowrate measurement.

The uncertainty in the plenum mass flowrates, as measured at the choked feed orifices, was estimated using the uncertainties in the $\Gamma_{feed,i}$ calibration and in the measurements of p_{0cm} and T_{0cm} . The uncertainty calculation method is described comprehensively by Povey et al. [12]. To 95% confidence, the bias uncertainty was $\pm 1.07\%$ and the precision uncertainty was $\pm 0.38\%$.

Table 3 lists the measured coolant mass flowrates, normalized by \dot{m}_{1N} , through each plenum at each of the three cooled test points

Table 3 Experimentally measured coolant mass flowrates for each plenum feed for each of the three cooled test points

Plenum	Normalized coolant mass flow rate, \dot{m}_c/\dot{m}_{1N} , %		
	Case A	Case B	Case C
1	0.327	0.442	0.704
2	0.492	0.666	1.017
3	0.381	0.516	0.788
4	0.427	0.580	0.882
Total	1.627	2.204	3.391

(cases A–C), as well as the total mass flowrates from all four plenums combined. The coolant mass flowrates have been scaled to the fully annular case (by a factor of 15). Values were averaged over at least two good runs at each test point. The total coolant mass flowrate was maintained to within $\pm 5\%$ of the target value during testing, demonstrating the level of run-to-run repeatability. The run-to-run variation was primarily due to pressure control issues associated with the coolant supply: the total coolant mass flowrate was effectively set by filling the coolant air reservoir to a set pressure prior to each run, and it was difficult to precisely set this pressure as this was a manual process and the reservoir leaked slightly.

The mass flowrate through each row of cooling holes was estimated using a similar technique to that used for plenum mass flowrates. The mass flowrate through row j supplied by plenum i can be calculated using

$$\dot{m}_{cj}(p_{0ci}/p_{ej}) = \frac{p_{0ci}}{\sqrt{T_{0ci}}} \Gamma_{row,j}(p_{0ci}/p_{ej}) \quad (10)$$

where $\Gamma_{row,j}$ is the steady flow capacity of the row, p_{0ci} and T_{0ci} are the measured coolant stagnation conditions within the plenum, and p_{ej} is the predicted static pressure at row exit (from time-averaged URANS simulation, nondimensionalized in terms of the turbine-inlet total pressure, then scaled using the turbine-inlet total pressure measured during the particular run). The row capacity characteristics, $\Gamma_{row,j}$, were measured experimentally via a series of blowdown tests (conducted in a separate facility) exhausting to the atmosphere, using the high-accuracy differential mass flowrate measurement technique devised by Kirollos and Povey [13]. The sensitivity of $\Gamma_{row,j}(p_{0ci}/p_{ej})$ to the Reynolds number changes and coolant gas properties was not accounted for, as the correction factor was estimated to be small in comparison with the overall uncertainty in the mass flowrate measurement.

For each row, a single time-averaged value of p_{ej} was used to calculate \dot{m}_{cj} . As a result, Eq. (10) does not account for two physical

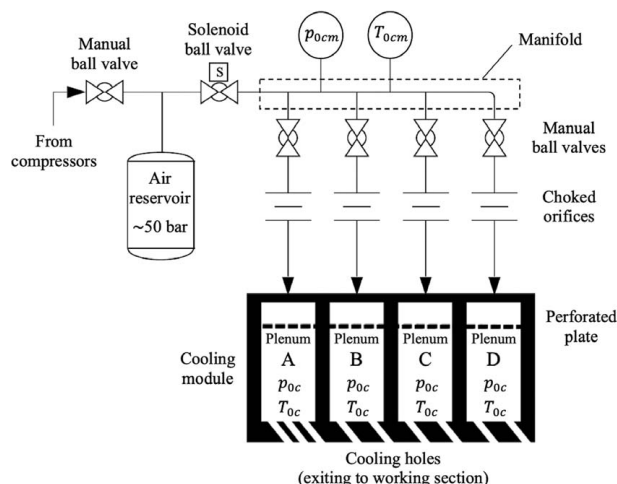


Fig. 6 Schematic of the experimental coolant supply system

effects that may influence \dot{m}_{ej} : first, the effect of circumferential variation on the hole exit static pressures along each row (e.g., those arising due to the HP/IP vane potential fields); second, the nonlinear mass flux characteristics of the cooling holes, which arise due to acoustic effects within the holes driven by temporal variations in the hole exit static pressure (e.g., due to rotor blade passing). With regard to the first effect, the row exit pressures were estimated using high-resolution survey measurements of the rotor over-tip casing static-pressure distribution without cooling. These measurements, presented in Ref. [11], showed no significant circumferential variation in the casing static pressure, suggesting that the error introduced by neglecting circumferential variation in the row exit static pressures would be relatively small. With regard to the second effect, shown by Collins and Povey [4], who first reported this phenomenon, these acoustic effects can result in time-averaged coolant mass flowrates that differ from those calculated using a steady capacity characteristic with time-instantaneous pressure ratios across the holes (the so-called quasi-steady mass flowrate). Nevertheless, URANS predictions reported by Collins et al. [3] showed for a similar cooling hole geometry that the difference between quasi-steady and truly unsteady mass flowrates was relatively small ($\sim 1\%$). Indeed, comparing the sum of all \dot{m}_{ej} (rows 1–9), calculated using Eq. (10), to the sum of all \dot{m}_{ci} (plenums 1–4) agreed to within 0.9% for all tests. This summation check across all results gives significant confidence to the results.

Figure 7 shows the measured mass flowrates through each row for each test point. Results have been averaged over several runs at each test point. For all test points, the mass flowrates of each of the leading three rows are approximately equal to each other. This is as expected, as these rows are all supplied by plenum 1 at the same stagnation conditions (of total pressure and temperature) and have similar row-average exit pressures (all are upstream of the rotor). Rows 4 and 5 also share a common plenum and thus exhibit similar trends. Rows 6 and 7 also share a plenum, but row 7 features half as many holes as row 6, explaining the lower mass flowrate of this row. Mass flowrates for rows 8 and 9 differ for the same reason.

Measurement Techniques and Instrumentation. Traverse measurements were conducted at rotor exit using three probes: a combined three-hole pneumatic (steady total pressure, Mach number, and yaw angle) and aspirated thermocouple probe (total temperature); and a miniature pitot probe (high-resolution total pressure); and miniature temperature probe (high-resolution total temperature). The combined three-hole and thermocouple probe had a 5.6-mm diameter tip, and both miniature probes 1.6-mm diameter tips. The larger probe has the advantage of a full calibration map (taking account of yaw angles) but the disadvantage of greater flow disturbance. Photographs of two of the probes are shown in Fig. 8.

The pitot probe has a 45-deg chamfer on the inlet diameter to reduce sensitivity to incidence angle (errors were smaller than 1% within a ± 12 -deg range of incidence angles [14]). Both probes

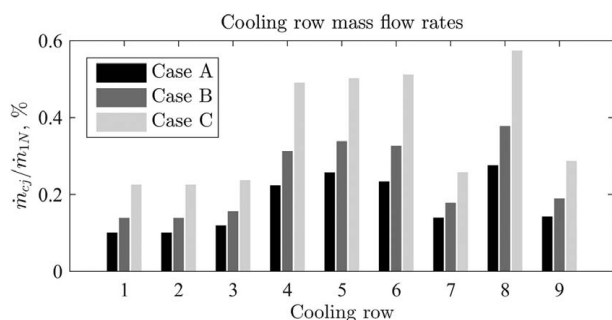


Fig. 7 Experimentally measured coolant mass flowrates through each row of casing effusion cooling holes for cooling flow test points A, B, and C

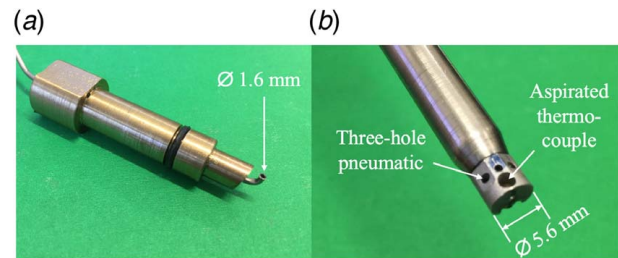


Fig. 8 Rotor-exit probes: (a) miniature pitot probe, and (b) traverse probe, featuring three-hole pneumatic probe and aspirated thermocouple

were angled at $+15$ deg with respect to the machine axis in order to approximately align with the average flow angle in the near-casing region of the passage.

The three-hole probe was calibrated over a Mach number range of 0.3–0.7 and a yaw angle range of ± 40 deg using the Oxford Probe Calibration Facility, described in Ref. [15]. The frequency responses of the three-hole probe and thermocouple probes measurements were independently estimated to be approximately 100 Hz, based on experimentally validated analytical predictions described in Refs. [16] and [17], respectively. Both temperature and pressure measurements were therefore low-pass filtered using a two-pole Butterworth filter at 90 Hz to reduce unphysical noise. For this type of probe and calibration procedure, typical uncertainties associated with the measurements of total pressure and total temperature (presented later) are $\pm 0.1\%$ and $\pm 0.4\%$, respectively, to 95% confidence. At the nominal traverse speed of 120 mm s^{-1} , this implies a radial resolution of approximately 1.2 mm or 2.9% span.

A pneumatic piston actuator was used to traverse the probe (in the radial direction, at a fixed circumferential location) through a range equivalent to approximately 20–100% span during the aerodynamically stable period of the run. The probe stem was sealed by a nitrile O-ring installed within the casing to prevent leakage from the working section. The probe traverse path was at an angle $+3.3$ deg from radial (where the angle is defined as positive in the direction of shaft rotation), and this was accounted for in data post-processing. All rotor-exit measurements were conducted at the same axial position: $x/C_{ax}^{tip} = 1.75$ measured from the rotor blade leading edge (LE). The traverse probe position was measured using a linear position sensor. An example trace is shown in Fig. 9 (black line). The start and end times of the measurement period are indicated by vertical broken lines. A typical traverse time was approximately 230 ms, which occurs within the stable region of the run.

Mid-span aerodynamic loading measurements were conducted on an HP vane instrumented with 16 CNC-drilled surface static pressure tappings of diameter 0.5 mm. The tappings were drilled at 50% span on both the pressure side (PS) and suction side (SS) of the vane. The instrumented vane was axially upstream of the

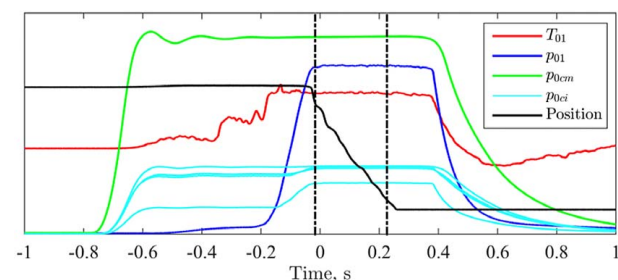


Fig. 9 Measured traces during a typical OTRF run, arbitrarily normalized in order to fit on common axes. The start and end times of the measurement period are indicated by vertical broken lines.

center of the cooled casing sector. Two additional static-pressure tapings were machined on the casing shortly downstream of the vane TE.

Experimental Results

Impact of Probe Size on Total Pressure Traverse Measurements. Before examining the radial profiles measured at the rotor exit, the impact of traverse probe disturbance on the flow is assessed by comparing results from both the multi-hole traverse probe and the miniature pitot probe. Figure 10 shows pitot measurements conducted at several discrete radial heights both with cooling (Case C) and without cooling, overlaid on three-hole probe measurements. Data from both probes are normalized in real time by the measured turbine-inlet total pressure to correct for small variations in p_{01} , and then time-averaged during the stable period of the run. The results from the pitot and three-hole probes are in reasonably good agreement in form and absolute level. Most importantly, the measured change in the total pressure profile with coolant introduction is similar for both probes. It was concluded that the impact of probe size was relatively small so far as the measurement of total pressure was concerned.

The measurements from individual probes were highly repeatable on a run-to-run basis, with the data virtually overlaying from repeat runs.

Rotor-Exit Traverse Measurements. Figure 11 presents rotor-exit traverse measurements of total pressure and total temperature. Measurements are shown both with and without cooling. With

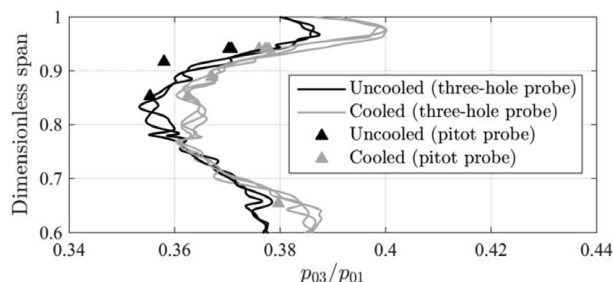


Fig. 10 Experimental measurements of total pressure at rotor exit using a traversing three-hole probe (diameter 5.6 mm) and a stationary miniature pitot probe (diameter 1.6 mm)

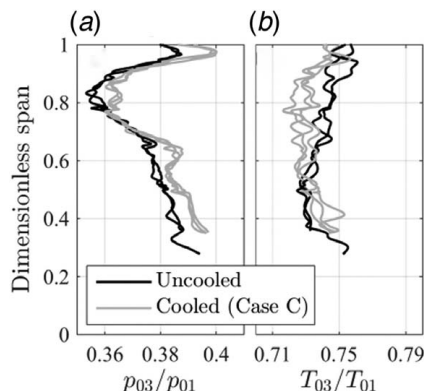


Fig. 11 Rotor-exit radial traverse measurements with cooling (Case C, $\dot{m}_c/\dot{m}_{1N} = 3.39\%$) and without cooling ($\dot{m}_c/\dot{m}_{1N} = 0$): (a) normalized total pressure and (b) normalized total temperature

cooling, traverse measurements were conducted only for Case C ($\dot{m}_c/\dot{m}_{1N} = 3.39\%$), which was expected to cause the most significant change to the flow. The local p_0 and T_0 measurements were normalized in real time by turbine-inlet p_{01} and T_{01} measurements, respectively, in order to correct for small temporal variations. Data from multiple runs are overlaid, showing a high level of repeatability between runs (traverse measurements were taken during the aerodynamically stable period of the run). Small variations in the profiles between runs at a given condition are likely due to unsteady fluctuations in the flow and the uncertainty of the probes, rather than due to the unsteady responses of the probes (as discussed, the raw data were filtered to eliminate this effect) or their potential-field interactions with the flow (which are expected to be small and should be consistent between runs).

The measured total pressure profile without cooling shows several features typical of rotor-exit flows. First, the profile is relatively flat between approximately 35% (lower extent of traverse) and 65% span, a region with relatively little influence from secondary flows. Second, a total pressure deficit is observed from approximately 65–90% span, corresponding to loss associated with the tip leakage and passage vortices (this observation is supported by CFD predictions shown later). Finally, a region of high total pressure is observed above 90% span (above the tip leakage vortex core).

With the introduction of coolant, the measurements show an increase in total pressure across the majority of the span covered by the traverse. At mid-span, the measured increase of +1.45% compares very well to the mean-line predictions of +1.54% (membrane model) and +1.47% (mixed-out model) at the same \dot{m}_c —see Table 1.

The total temperature profiles show a small but measurable reduction in total temperature (of up to approximately 10 K) from approximately 70–90% span with the introduction of coolant. This observation is consistent with the transport of coolant away from the casing by the action of the tip leakage vortex and possibly the upper passage vortex, as suggested in Ref. [1] based on rotor-exit traverse measurements and in Ref. [3] based on 3D URANS calculations.

In summary, traverse measurements show that coolant introduction causes significant global changes in the turbine operating point, in addition to local changes in the tip secondary flow structures. This is evidenced by the fact that the total pressure increase is not limited to the near-casing region but instead extends across much of the passage height.

High-Pressure Vane Loading Measurements. HP vane loading measurements were conducted with and without cooling, in order to verify the result of the mean-line prediction that the vane exit static pressure, p_2 , increases with the introduction of coolant. Results are shown in Fig. 12, where the data from three runs at each test point have been averaged. When normalized by

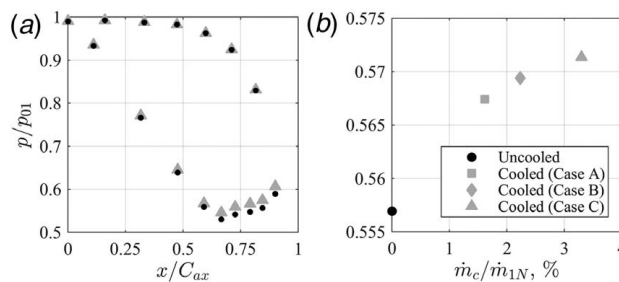


Fig. 12 Experimentally measured surface static pressures, normalized by turbine-inlet total pressure, with and without cooling: (a) HP vane mid-span static pressure distribution, and (b) HP vane-exit casing pressure measured using a single tapping near the center of cooled sector

the turbine-inlet total pressure, data from different runs collapsed with excellent agreement.

Figure 12(a) shows HP vane mid-span loading measurements with cooling (Case C) and without cooling. On the PS, the vane loading is unaffected by the introduction of coolant. On the early SS ($0 < x/C_{ax} < 0.6$), there is a slight increase in static pressure with cooling, while on the aft SS ($0.6 < x/C_{ax} < 1$), there is a marked increase in static pressure. These measurements suggest a reduction in HP vane pressure ratio with casing effusion cooling. As discussed previously, it is expected that this effect arises as a result of the coolant occupying a small fraction of the rotor capacity (effectively causing a blockage in the rotor). The measured static pressure increase at the furthest downstream tapping location ($x/C_{ax} = 0.9$) is 2.95%, which compares well with the predictions of the mean-line model: p_2 increases of 2.68% (membrane model) and 3.05% (mixed-out model). These predictions are listed and compared to the experimental results in Table 4 for the same \dot{m}_c .

Figure 12(b) shows the static pressure on the HP vane-exit casing (measured using a single tapping) for the uncooled tests and for three cooled tests with increasing \dot{m}_c (cases A–C). For increasing \dot{m}_c , p_2 increases, a result which is consistent with the mid-span loading measurements. For Case C, the static pressure increase on the casing was 2.64%, which is similar in magnitude to that on the vane mid-span surface at $x/C_{ax} = 0.9$ (2.95%). This supports the conclusion that the mean-line model predictions of p_2 are in good agreement with the experimental measurements. As discussed previously, the p_2 increase is expected to cause a reduction in rotor incidence and an increase in $p_{02,rel}$.

Numerical Setup

Unsteady 3D numerical simulations were also conducted to help understand the mechanisms of interaction of the casing effusion cooling flows with the main flow, and the impact on tip leakage structure, downstream loss, and stage operating point. The full 1.5-stage domain was modeled, as opposed to the rotor domain only, so that the conditions at rotor inlet and exit could vary with the cooling mass flowrate, \dot{m}_c .

Solver and Mesh. The Rolls-Royce in-house HYDRA suite [18] was used for all CFD simulations. The solver is based on pre-conditioned time marching of the RANS equations. The RANS equations are discretized in space using a second-order edge-based finite-volume scheme and integrated in time using a multistage Runge–Kutta scheme. The $k-\omega$ shear stress transport model is employed for RANS closure. Wall functions were imposed on the solid boundaries.

The LEMCOTEC 1.5-stage turbine blade-count ratio of 2:3:1 allowed a periodic computational domain with a sector of only 18 deg. A block-structured mesh was generated for this domain using the Rolls-Royce in-house Parametric Design Rapid Meshing (PADRAM) system [19]. The same block-structured mesh was used for all cooled and uncooled simulations, with 5.3 million, 3.2 million, and 1.9 million nodes per passage in the HP vane, HP rotor, and IP vane, respectively (22.2 million nodes in total). The rotor blade-tip gap meshed with 40 cells in the radial direction. The average y^+ values were less than 20 in the HP and IP vane domains and less than five in the rotor domain. For full-annulus unsteady simulations, the mesh density was slightly

reduced for each passage and a total of 406 million nodes were used.

Boundary Conditions. At turbine inlet, uniform boundary conditions of p_0 and T_0 were imposed at the design values listed in Table 2, with a uniform turbulence intensity of 10%. The IP vane-exit static pressure was imposed using a linear radial profile matched at the endwalls to experimental measurements. Adiabatic walls were imposed at the vane, blade, and endwall surfaces.

Cooling Source-Term Model. Casing effusion cooling (48 holes per rotor passage; 144 holes per three-blade-sector) was modeled using a source-term technique: source terms (for mass flux, momentum flux, and total enthalpy flux) were introduced to the governing equations at mesh nodes located within circumferentially continuous “strips” at the axial locations of the nine cooling rows in the experimental geometry. Although the strip model is a crude approximation of the real situation, in particular for the unsteady simulations, this study is primarily concerned with the bulk (large-scale) blade-row mismatching effects rather than the detailed (small-scale) coolant injection aerodynamics. Furthermore, the unsteady simulations are used only to predict the importance of cooling a sector of the annulus rather than the full annulus. Therefore, since the strip model is expected to capture these bulk-flow effects, it was assumed to be an acceptable simplification for the present computational study.

The settings for the cooling strip model were derived using OTRF measurements. For each cooling strip, the mass flowrate (circumferentially uniform) matched the experimental (estimated) values for each cooling row presented in Fig. 7 and the total enthalpy was based on the measured coolant total temperature (averaged over all runs). The total momentum for each strip was estimated as follows. First, the hole exit Mach number, M_{ce} , was estimated for each row using the measured coolant mass flowrate and nominal hole exit areas (identical for all rows, based on 0.50-mm hole diameters). The flow through each hole was assumed isentropic. Thus, the hole-exit static pressure, p_{ce} , and static temperature, T_{ce} , could be calculated using isentropic relations. The coolant density, ρ_{ce} , and velocity, v_{ce} , at hole exit were then calculated using the gas equation of state ($\rho_{ce} = p_{ce}/RT_{ce}$) and hole-exit Mach number ($v_{ce} = M_{ce}\sqrt{\gamma RT_{ce}}$), respectively. The momentum for each row was calculated as $\rho_{ce}v_{ce}^2$. Cylindrical components of momentum were calculated for each strip using the hole orientation angles (extracted from the CAD model of the cooling module), which were identical for all holes in a given row. The strips were also smeared radially up to a penetration depth (measured from the casing surface) arbitrarily set as half of the tip gap. Thus, the source terms were technically imposed over a 3D volume rather than a two-dimensional (2D) surface. A numerical study into the sensitivity of the results to penetration depth suggested some degree of sensitivity of the local flow structure (e.g., tip leakage) but comparatively little sensitivity of the change in operating point, which is the primary focus of the present investigation.

For the full-annulus simulations described in the following section, HP vane film cooling was also implemented using a similar technique. However, HP vane film cooling was not implemented in the OTRF experiments and is not the focus of the present investigation. Since the HP vane film cooling conditions were the same for all full-annulus simulations conducted, comparisons between simulations with different casing effusion cooling mass flowrates are not thought to be significantly affected by this difference between experiment and CFD setup: our main focus is relative changes in turbine operating point and aerodynamics due to coolant introduction, not absolute validation of the CFD model.

Convergence Criteria. Steady simulations were run until convergence was reached. Such a condition was defined as the point

Table 4 Change in HP vane-exit casing static pressure with cooling (Case C, $\dot{m}_c/\dot{m}_{IN} = 3.39\%$), as measured in the OTRF and predicted by the two mean-line models

	OTRF	Membrane model	Mixed-out model
Change in p_2	+2.95%	+2.68%	+3.05%

at which the predictions of stage capacity, reaction, efficiency, and loading, in addition to the maximum root-mean-square of the solution residuals, showed no change with additional iterations. Unsteady simulations were run until the temporal periodicity of the solution, measured using the same criteria as for steady simulations, was observed for at least one full (360-deg) rotation of the rotor. At each physical time-step in the unsteady solution, pseudo-steady convergence was confirmed within 15 internal iterations.

Computational Results

Comparison With Rotor-Exit Traverse Measurements:

Uncooled Results. We first discuss the level of agreement between the measured (Fig. 11) and CFD-predicted (Fig. 13) radial profiles of p_{03} and T_{03} along the path of the traverse probe without cooling (black trends in Fig. 13). The measured and predicted p_{03} profiles are generally in good agreement: a region of low total pressure is observed above 80% span (due to secondary flow loss) and a region of comparatively constant total pressure is observed between 35 and 50% span (due to the relative absence of secondary flow influence). However, the measured and predicted p_{03} profiles show a different radial position of the tip leakage vortex (low total pressure trough near the casing) with peak loss observed at ~80% span in the measured profile and at ~90% span in the predicted profile. This disagreement (equivalent to ~4 mm of span) is above the effective probe resolution in the span direction (estimated to be ~1.6 mm, taking into account the span-wise extent of the probe holes) and may be the result of flow interaction with the probe tip in the near-casing region (difference in flow structure compared to the calibration environment) or due to failure of the CFD model to accurately predict the secondary flow in this region.

The predicted T_{03} profile shows a significantly greater degree of radial non-uniformity compared to the measured profile. It is noted, however, that quantitative comparison is complicated by the presence of HP vane film cooling in the CFD model (not present in the experiments).

Comparison of Cooled-Sector and Cooled-Annulus Computational Fluid Dynamics Simulations. We now compare CFD results from cooled-sector simulations (24-deg sector) and

cooled-annulus simulations, to determine the extent to which cooled-sector experimental results can be taken as representative of the result for an entire cooled annulus. In particular, we consider the impact on local (to the cooled-sector) rotor-exit traverse measurements. To this end, full-annulus 1.5-stage URANS calculations were performed for three situations: (i) no cooling, (ii) casing effusion cooling applied to a 24-deg sector, and (iii) casing effusion cooling applied to the entire annulus. For the two cooled simulations, the coolant mass flowrate was set to $\dot{m}_c/\dot{m}_{1N} = 2.20\%$ (Case B). In all three simulations, a full annulus of 20 HP vanes and 60 rotor blades was modeled. A sliding mesh interface was employed between the HP vane and rotor domains, while a mixing plane was used between the rotor and IP vane domains (only a single IP vane passage was modeled).

Figure 13 shows predicted radial profiles of p_{03} and T_{03} extracted along the traverse path for the uncooled, cooled-sector, and cooled-annulus simulations. While the predicted profiles with and without cooling show significant differences (discussed later), little difference is observed between the cooled-sector and cooled-annulus profiles. This result suggests that at the location of the traverse probe, the effects of cooling only a finite sector rather than the full annulus are insignificant. Therefore, the traverse measurements presented in Fig. 11 can be considered representative of the fully periodic environment.

Uncooled-Annulus Versus Cooled-Annulus Results. We now compare the measured (Fig. 11) and predicted (Fig. 13) changes to the p_{03} and T_{03} profiles along the probe path due to coolant introduction. Both the measurements and predictions show an increase in p_{03} at most span locations with cooling. At mid-span, the predicted total pressure increase (with respect to uncooled) is +0.98% with $\dot{m}_c/\dot{m}_{1N} = 2.20\%$, which is consistent with both the mean-line model predictions (+1.20% for the membrane model and +0.99% for the mixed-out model with the same \dot{m}_c) and the experimental traverse measurements at mid-span (+1.45% with $\dot{m}_c/\dot{m}_{1N} = 3.39\%$) taking the scaling with cooling flow into account. Furthermore, the predictions show that the p_{03} increase extends below the lower limit of the traverse measurements (~35% span). Both the measurements and predictions show a reduction in T_{03} around 80% span with cooling, likely indicating that the casing coolant is substantially entrained in the tip leakage

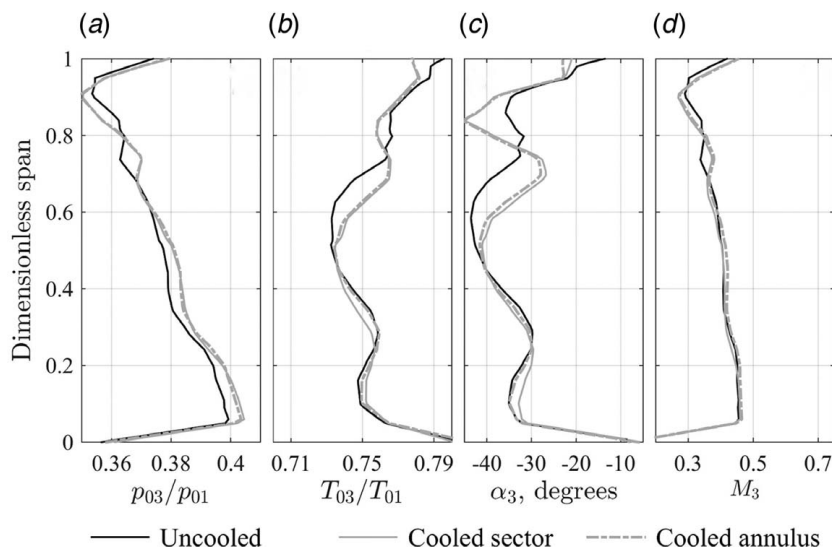


Fig. 13 Predicted radial profiles at rotor exit along the path of the traverse probe: (a) normalized total pressure, (b) normalized total temperature, (c) yaw angle, and (d) Mach number. Data are presented for three cooling configurations: (i) uncooled, (ii) cooled sector, and (iii) cooled annulus. For both cooled simulations, the coolant mass flowrate per cooled sector was $\dot{m}_c/\dot{m}_{1N} = 2.20\%$ (Case B).

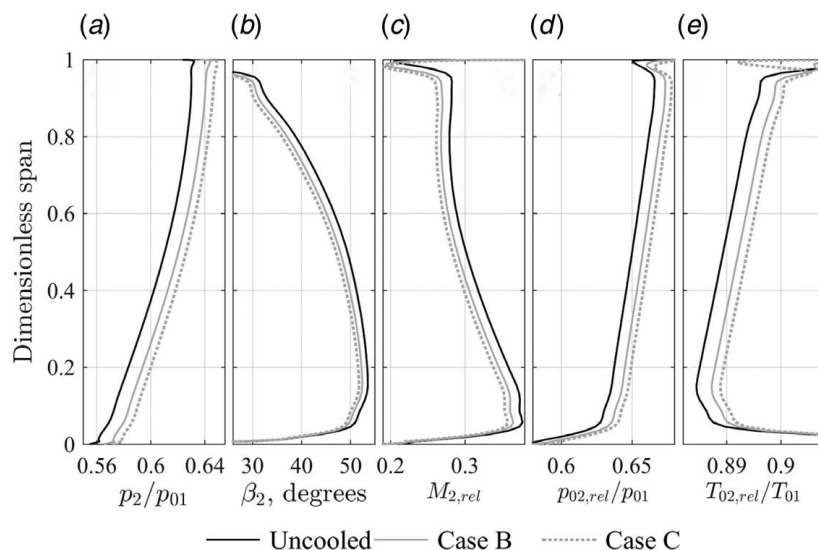


Fig. 14 Predicted circumferentially mass-averaged profiles at rotor inlet with cooling (cases B and C) and without cooling: (a) normalized static pressure, (b) relative yaw angle, (c) relative Mach number, (d) normalized relative total pressure, and (e) normalized relative total temperature

vortex. Further quantitative comparison between the measured and predicted T_{03} profiles is complicated by the presence of HP vane film cooling in the CFD model (which was not present in the experiments).

Effect on Effusion Cooling on Rotor-Relative Flow. We now compare results from RANS simulations without cooling and with two particular coolant mass flowrates applied over the entire annulus: $\dot{m}_c/\dot{m}_{1N} = 2.20\%$ (Case B) and $\dot{m}_c/\dot{m}_{1N} = 3.39\%$ (Case C). Results from these three simulations are presented in Fig. 14, which shows radial profiles of circumferentially averaged static pressure p_2 , relative yaw angle, β_2 , relative Mach number, $M_{2,rel}$, relative total pressure, $p_{02,rel}$, and relative total temperature, $T_{02,rel}$, at rotor inlet. The results show that for both of the coolant mass flowrates investigated, p_2 is increased (due to the reduction in HP vane mass flowrate) across the entire span by an

approximately uniform amount, the magnitude of the increase being proportional to \dot{m}_c . Similarly, the results show approximately uniform reductions in β_2 and $M_{2,rel}$ and increases in $p_{02,rel}$ and $T_{02,rel}$ across the entire span, where the changes are again proportional to \dot{m}_c (for reasons discussed in the mean-line analysis section of this paper).

The RANS predictions discussed above are consistent with the mean-line model predictions presented earlier. For example, for Case C, the RANS model predicted a span-averaged change in p_2 of +2.66%, which is in directional agreement with the mean-line model predictions of +1.69% (membrane model) and +3.05% (mixed-out model)—see Table 1. At the same \dot{m}_c , the RANS model predicted a span-averaged change in β_2 of -4.65 deg, which is in good agreement with the mixed-out mean-line model prediction of -4.95 deg at Station 2a, i.e., before coolant injection. The membrane model predicted a change in β_2 (for the mainstream

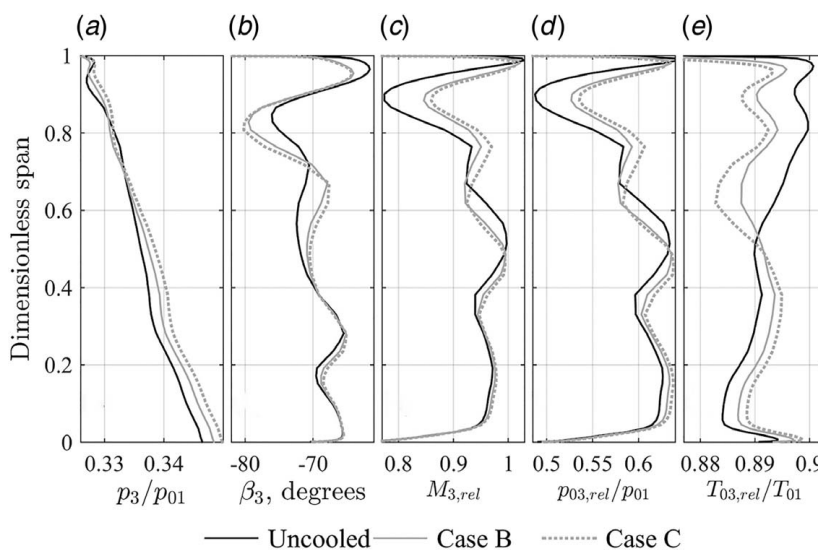


Fig. 15 Predicted circumferentially mass-averaged profiles at rotor exit with cooling (cases B and C) and without cooling: (a) normalized static pressure, (b) relative yaw angle, (c) relative Mach number, (d) normalized relative total pressure, and (e) normalized relative total temperature

flow) of only -1.44 deg, which is smaller but still in directional agreement with the RANS prediction.

Figure 15 presents the corresponding radial profiles at the rotor-exit plane. The results show that with cooling, there is an increase in p_3 across most of the passage span with cooling, the effect being greatest toward the hub. Furthermore, the p_3 increase is proportional to \dot{m}_c . For Case C, the span-averaged change in p_3 is $+0.68\%$, which is in directional agreement with the mean-line model predictions of $+1.53\%$ (membrane model) and $+1.26\%$ (mixed-out model).

The radial profiles of β_3 are for all simulations more non-uniform than the corresponding profiles at rotor inlet as a result of the rotor secondary flows. Consider first the results without cooling. The flow above 80% span is dominated by the tip leakage vortex, which causes reduced (in terms of absolute value) β_3 between 90 and 100% span and increased β_3 between 80 and 90% span (with respect to the mean). Below the tip leakage vortex is the counter-rotating upper passage vortex, which causes reduced β_3 between 60 and 75% span and reinforces the tip leakage vortex to cause increased β_3 around 80% span (again with respect to the mean).

For both cooled simulations, the absolute value of β_3 is increased (by up to ~ 5 deg) between 90 and -100% span, which is consistent with a reduction in strength of the tip leakage vortex. This result is perhaps unsurprising for two reasons: first, the momentum of the coolant—in general—opposes (in direction) the momentum in the tip leakage flow; second, the blockage effect (reduction in tip leakage mass flow) results from coolant injection into the tip gap (see discussions of these effects in Refs. [3,5,6]). It is also noticeable that in the region between 60% and 80% span, the magnitudes of positive and negative deviations in β_3 from the mean are increased. This suggests that the upper passage vortex is strengthened (by up to ± 5 deg). The span-wise location also appears to be displaced (by up to 5% of the span) towards the hub, and a larger overall fraction of the span is affected by the secondary flow, suggesting an increase in size (in addition to strength) of the upper passage vortex. It has been shown through cascade testing with simulated relative casing motion that an effect of the tip leakage vortex is to weaken, displace, and deform the upper passage vortex through shear interaction [20,21]. Thus, it is possible that the weakening of the tip leakage vortex with cooling contributes to the strengthening and displacement of the upper passage vortex.

The radial profiles of $p_{03,rel}$ show that there is an increased $p_{03,rel}$ across most of the span with the introduction of cooling. The increase is greatest between 80 and 90% span (up to 9.1%), where the increase is significantly greater than the $p_{02,rel}$ increase at rotor inlet (approximately 1.8%). This result suggests a significant reduction in a loss in the region of the tip leakage vortex. Below mid-span, the relative total pressure increase is approximately equal to that at rotor inlet, indicating no significant change in the loss. Between 50 and 60% span, there is a reduction in relative total pressure (of up to 4.1%), which is consistent with an increase in loss associated with the upper passage vortex.

The changes to the radial profile of $M_{3,rel}$ with cooling are similar to those for $p_{03,rel}$. Below mid-span, however, the increases in $M_{3,rel}$ are comparatively smaller than for $p_{03,rel}$ because of an increase in static pressure in the hub region with coolant introduction.

The $T_{03,rel}$ profiles show significant reductions in relative total temperature above mid-span with cooling. The greatest reductions are observed at 65% span (up to 1.3% for Case C) and 90% span (up to 1.1% for Case C), indicating that coolant has been transported into both the tip leakage and upper passage vortices. Below mid-span, the observed $T_{03,rel}$ increases result directly from the $T_{02,rel}$ increases at the rotor inlet.

Effect on High-Pressure Vane and Rotor Blade Loading. Figure 16 shows time-averaged predicted loading distributions on the HP vane and rotor blade at 10%, 50%, and 90% span with effusion cooling ($\dot{m}_c/\dot{m}_{1N} = 2.20\%$, Case B) and without effusion cooling. The HP vane loading distributions (left-hand column) show increased static pressure on the late SS ($0.6 < x/C_{ax} < 1$) and little change elsewhere on the vane. Thus, there is a reduction in the loading of the

aft part of the vane, which is consistent with a reduction in the vane pressure ratio. As discussed previously, this results from coolant occupying a small fraction of the rotor capacity (effectively causing blockage). The CFD-predicted change in mid-span static pressure at $x/C_{ax} = 0.9$ is 1.79%, which is in reasonable agreement with the experimental measurement (2.16%) at the same \dot{m}_c .

The rotor blade loading distributions (right-hand column) show increased static pressure on the forward half of both the PS and SS of the blade. The increases in peak static pressure (LE region) at 10%, 50%, and 90% span were 1.16%, 1.19%, and 1.35%, respectively. These predictions are consistent with an increase in $p_{02,rel}$ at rotor inlet, which was also predicted by the mean-line model. At the same \dot{m}_c , the $p_{02,rel}$ increase predicted by the mean-line model was 1.23% (membrane model) and $+1.03\%$ (mixed-out model), in reasonable agreement with the CFD predictions.

At 10% and 50% span, there is almost no change in TE static pressure: the static pressure increase observed on the forward part of the blade appears to be offset by an increase in flow expansion through the rotor at these span locations. At 90% span, there is a very significant change to the SS static-pressure distribution in the range $0.44 < x/C_{ax} < 1$. This is likely a result of the altered tip leakage and secondary flow structures near the blade tip, which was also indicated in Fig. 13.

Discussion. The mean-line model, CFD, and experimental results suggest two distinct effects on the HP stage aerodynamics arising from the introduction of rotor-casing effusion cooling. The first is a *global* change in stage operating point, with increased mid-stage static pressure which uniformly affects the velocity triangles at rotor inlet and exit. This global effect appears to be reasonably well-predicted by simple one-dimensional (1D) mean-line calculations. The second is a *local* change to the tip leakage and secondary flow structures, which are largely confined to the regions above mid-span. Prediction of this local effect cannot be achieved by

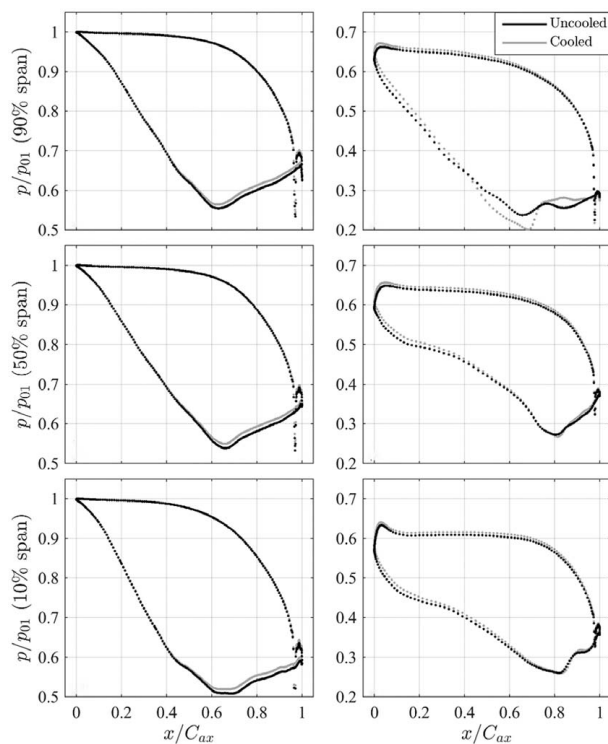


Fig. 16 Predicted loading distributions on the HP vane (left-hand column) and rotor blade (right-hand column). Data are presented at 10% span (bottom row), 50% span (middle row), and 90% span (top row) with cooling ($\dot{m}_c/\dot{m}_{1N} = 2.20\%$, Case B) and without cooling.

simple mean-line calculations but is captured in experimental data and 3D CFD.

Our results suggest that the (local) total pressure loss associated with the tip leakage vortex is reduced with cooling. In contrast, the upper passage vortex appears to be strengthened with cooling, but the change in loss is less clear. Furthermore, while our results suggest that the (global) change in operating point may cause reduced loading of the HP vane, and therefore mild loss reduction, there is an increase in rotor pressure ratio, which should be expected to increase loss. In the following section, we assess the overall effect of both global and local effects on stage performance and attempt to estimate the relative contributions of each.

Effect on Turbine Performance. Figure 17(a) presents predicted changes in the turbine-inlet mass flowrate and total turbine mass flow rate (coolant plus mainstream) for RANS simulations with two coolant mass flowrates (cases B and C) with respect to the uncooled simulation (Case U). The predicted changes in mass flowrate are in good agreement with the mean-line model (see Fig. 1): with increasing \dot{m}_c , the trends show a decrease in turbine-inlet mass flowrate and a comparatively large increase in total turbine mass flowrate.

Figure 17(b) presents predicted changes in turbine power output with cooling. There is virtually no change in \dot{W} for Case B and a small change of only -0.17% for Case C. This result is somewhat at odds with the mean-line model predictions (Fig. 3 and Table 1). For $0 < \dot{m}_c/\dot{m}_{1N} < 4$, the membrane model predicted a fairly steady decrease in \dot{W} for the mainstream flow (-1.73% for Case C), and when work done by the coolant was accounted for, the net power output increased ($+0.59\%$ for Case C). Meanwhile, the mixed-out model predicted a decreasing trend in \dot{W} (-2.34% for Case C) over the range of \dot{m}_c considered. Given that the two mean-line models were intended to represent two opposite extremes (no mixing and instantaneous/complete mixing of the coolant and mainstream) and given also that neither mean-line model captures changes in tip leakage flow structure, the discrepancy between mean-line and RANS predictions, whilst disappointing, is perhaps not entirely unexpected.

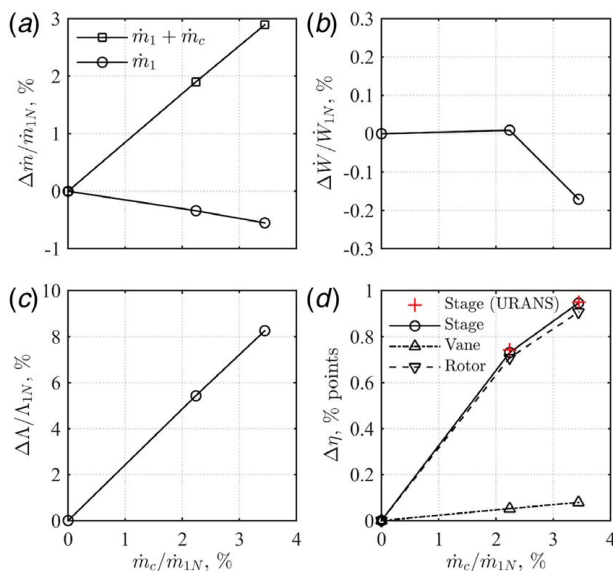


Fig. 17 Predicted performance changes for 1.5-stage RANS simulations with two coolant mass flowrates (cases B and C) with respect to the uncooled simulation (Case U): (a) changes in turbine inlet mass flowrate and total turbine mass flowrate (coolant plus mainstream), (b) change in turbine power output, (c) change in HP stage reaction, and (d) absolute change in efficiency of the HP stage (URANS predictions overlaid for comparison), vane, and rotor

Figure 17(c) presents predicted changes in mass-averaged HP stage reaction with cooling. Reaction increases linearly by approximately 2.4% for every 1% increase in \dot{m}_c/\dot{m}_{1N} over the range considered. The trend is in directional agreement with both mean-line model predictions—see Fig. 3(f). Quantitative agreement with the mixed-out model is better than that with the membrane model. For $\dot{m}_c/\dot{m}_{1N} = 2.20\%$ (Case B), the RANS model predicts a 5.4% increase in reaction, compared to 4.2% with the mixed-out model and 2.3% with the membrane model. Thus, the RANS predictions suggest that of the two mean-line models, the mixed-out model is more accurate at predicting the redistribution of expansion throughout the stage.

To investigate whether cooling causes an overall improvement in the HP stage expansion process, we use mechanical work potential efficiency [22]. The efficiency was evaluated by calculating the local rate of entropy creation per unit volume and integrating over the volume of interest. This procedure allowed the contributions to total stage efficiency deficit due to the vane and rotor rows to be separated.

Figure 17(d) presents predicted absolute changes in HP stage efficiency with cooling. The trend shows that, for the \dot{m}_c values considered, stage efficiency increases as \dot{m}_c increases. For cases B and C, the stage efficiency changes are $+0.73\%$ and $+0.95\%$, respectively. Overlaid are URANS-predicted efficiencies, which are in excellent agreement with the RANS predictions (to within 0.01% points), suggesting that the effects of unsteady blade-row interactions are small in this situation. The predicted changes in HP vane and rotor efficiency are also plotted. Both efficiencies are observed to increase with increasing \dot{m}_c , but the increase in vane efficiency is small in comparison with the increase in rotor efficiency.

A key question is how much of the predicted stage efficiency increase results from the global change in stage operating point and how much results from a local improvement in blade-tip aerodynamics (such as possible spoiling of the tip leakage flow). Ideally, this question would be answered using an uncooled simulation with the stage operating point perfectly matched to the cooled simulation; the efficiency change with respect to the uncooled simulation would indicate the efficiency change due to the (global) change in stage operating point alone, allowing the efficiency change due to (local) changes in blade-tip aerodynamics to be inferred. However, the introduction of additional mass (the effusion cooling flow) midway through the turbine makes the construction of a perfectly matched simulation impossible.

To estimate the change in efficiency due to the change in stage operating point alone, a performance characteristic could be generated from multiple CFD simulations run at a range of stage operating points around the design point. Neglecting relatively weak Reynolds number effects—which could likely be reasonably well estimated using empirical correlations—the corrected speed and pressure ratio could be varied for these simulations. A surface of predicted efficiency could then be plotted over this 2D space. The efficiency interpolated at the cooled operating point would then allow a reasonable estimate for the efficiency impact due to the change in operating point alone. Alternatively, single-row simulations of the HP vane and rotor rows could be run uncooled with row-inlet and row-exit boundary conditions set to the values obtained from the effusion-cooled 1.5-stage simulation. The stage efficiency calculated using these single-row solutions would—again—provide a reasonable estimate of the likely performance impact associated with the change in operating point alone (i.e., associated with the change in stage operating point with coolant injection, but discounting the local changes in secondary flow structure and local mixing effects).

Single-row RANS simulations of the HP vane and rotor were conducted as outlined earlier. We refer to the full-stage *proxy-solution* obtained by combining these single-row solutions as Case U2. The RANS model configuration and boundary condition setup corresponding to cases U, U2, and B are summarized in Table 5. Setup and results for cases U and B have been discussed

Table 5 Setup of full-stage and single-row RANS simulations used to estimate the efficiency change contributions due to global and local effects of coolant injection

Case	\dot{m}_c/\dot{m}_{1N}	Model config.	Boundary conditions
U	0%	Full 1.5-stage	$p_{01}, T_{01}, \alpha_1, \beta_1, p_4$
U2	0%	HP vane only	$p_{01}, T_{01}, \alpha_1, \beta_1, p_2$
		HP rotor only	$p_{02,rel}, T_{02,rel}, \alpha_{2,rel}, \beta_2, p_3$
B	2.2%	Full 1.5-stage	$p_{01}, T_{01}, \alpha_1, \beta_1, p_4$

previously; the full 1.5-stage domain was modeled and the boundary conditions at HP vane inlet and IP vane exit were imposed. Case U2 comprises an HP vane-only simulation with inlet and exit boundary conditions (1D radial profiles) extracted from Case B and an uncooled rotor-only simulation with inlet and exit boundary conditions (1D radial profiles) extracted from Case B.

Figure 18 presents predicted HP stage efficiency deficit for cases U, U2, and B. Efficiency deficit is computed as the lost power in each blade row as a fraction of the isentropic power output of the turbine; the vane and rotor efficiency deficit are summed to give the full-stage efficiency deficit. Our analysis is now progressed via three comparisons: U and B; U and U2; and U2 and B.

Comparing cases U and B allows the efficiency change due to both global and local effects of coolant introduction to be inferred. As discussed with reference to Fig. 17(d), there is a significant increase in stage efficiency (0.73% points), or corresponding reduction in efficiency deficit, due predominantly to an increase in rotor efficiency (of 0.70% points).

Comparing cases U and U2 allows the efficiency change due to the global effects to be inferred. There is a small increase in stage efficiency of 0.11% points, which results from small increases in both the vane and rotor efficiencies (of 0.06% points and 0.04% points, respectively). We conclude that the changes in the efficiency with cooling due to global effects alone (stage operating point changes) are small.

Comparing cases U2 and B allows the efficiency change due to local effects alone to be inferred. There is a significant increase in stage efficiency of 0.62% points due predominantly to an increase in rotor efficiency (of 0.66% points). We conclude that the changes in the efficiency with cooling due to local effects alone (e.g., changes in mixing, secondary flow, and tip-leakage spoiling), and discounting stage operating point changes, account for the majority of the overall efficiency change. That is, local effects predominate over global effects.

Taken together, the predictions suggest that both the global and local effects of coolant injection contribute to an increase in overall stage efficiency. Local effects appear to be approximately six times more significant than the global effects, however. This result is perhaps surprising, given the considerable changes in blade-row matching (see Figs. 14 and 15) and stage reaction (see

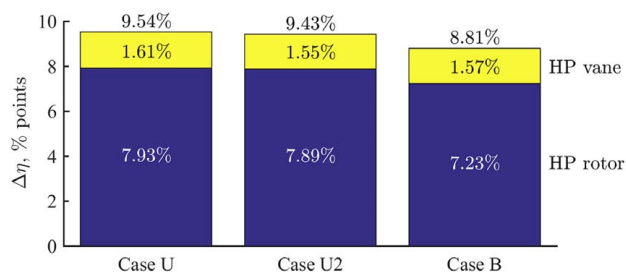
**Fig. 18 Predicted efficiency deficit comparisons: (U) uncooled; (U2) single-row proxy-solution with stage operating point of cooled Case B, (B) cooled Case B with $\dot{m}_c/\dot{m}_{1N} = 2.20$. Results are separated into vane and rotor components.**

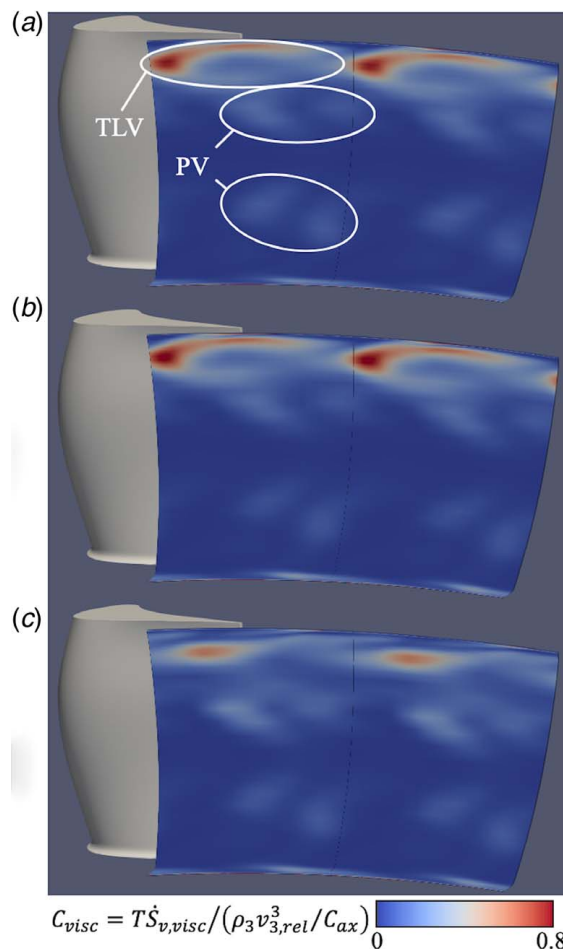
Fig. 17(c)). It is noted, however, that in our particular turbine design the rotor aerodynamic performance is relatively insensitive to incidence angle (due to the relatively large radius of the rotor LE—see Fig. 4). Thus, the effect is plausible, even though coolant injection changes the stage operating point in such a manner as to decrease rotor incidence angles. The predictions further suggest that the reduction in a loss in the rotor due to coolant introduction is significantly greater than that in the vane.

To provide a qualitative understanding of the loss changes in the rotor, we introduce a dimensionless viscous dissipation coefficient

$$C_{visc} = \frac{T\dot{S}_{v,visc}}{(\rho_3 v_{3,rel}^3 / C_{ax})} \quad (11)$$

where $\dot{S}_{v,visc}$ is the local rate of entropy generation per unit volume. The term in the numerator may be interpreted as the *lost power* due to viscous shear stress being converted to heat at the local static temperature, T . The term in the denominator, which is related to the kinetic energy flux exiting the rotor, is calculated using the mean density and mass-mean relative velocity at the rotor-exit plane. Figure 19 presents RANS-predicted area contours of C_{visc} at the rotor-exit plane for cases U, U2, and B.

For Case U, clear high-loss regions are observed at the locations of the TLV and passage vortices PVs; the strongest dissipation is associated with the tip leakage vortex. For Case U2, there is a slight increase in TLV loss, although the general structure of the loss contours is similar to that of Case U. This result is consistent

**Fig. 19 Predicted contours of dimensionless viscous dissipation coefficient at rotor exit: (a) Case U, (b) Case U2, and (c) Case B**

with the small increase in pressure ratio across the rotor, which can be expected to strengthen the tip leakage flow and resulting TLV. There is a slight reduction (almost imperceptible) in loss associated with the lower PV, which could be due to the reduction in rotor incidence angle.

For Case B, there is a significant loss reduction in the tip leakage vortex compared to cases U and U2. Furthermore, the structure of the TLV loss contours is significantly altered, with the dissipation occurring in a more confined region and closer to the blade SS. These results are consistent with a reduction in TLV strength due to blockage of the tip leakage flow, as was suggested by the radial profiles of yaw angle shown in Fig. 15. There is also a slight increase in loss associated with the upper PV, which is consistent with an increase in strength of the PV, as was suggested in Fig. 15. The loss contours associated with the lower PV are virtually unchanged with respect to Case U2, as should be expected given that the rotor-inlet and rotor-exit boundary conditions are identical for these simulations and the influence of the TLV in this region is small.

Overall, the C_{visc} contours of Fig. 19 support the conclusions that coolant introduction causes a significant improvement to the blade-tip aerodynamics and that the local effect on the tip leakage and secondary flow structures is much more significant than the global effect of the stage operating point change.

Conclusions

The effect of HP rotor-casing effusion cooling on the operating point and performance of a 1.5-stage turbine has been investigated via 1D mean-line modeling, rotating turbine experiments at engine-representative conditions, and 3D CFD simulations. The primary objective of the investigation was to—perhaps for the first time—clearly separate the performance changes due to local (e.g., coolant mixing and secondary flow changes) and global effects (e.g., stage operating point changes) of coolant introduction.

Our mean-line model is capable only of analyzing global changes caused by stage-matching effects (pressure ratio changes through a 1.5-stage machine). The following key effects were predicted with the introduction of effusion cooling (over the engine-realistic range $0 < \dot{m}_c/\dot{m}_1 < 4\%$) at a fixed turbine-inlet conditions, 1.5-stage pressure ratio, and shaft speed: (i) the static pressures at HP vane and rotor exit increased as a result of the cooling mass introduction; (ii) the HP vane pressure ratio decreased as a result of the coolant occupying a small fraction of the rotor capacity (effectively causing blockage in the rotor); (iii) this caused the turbine-inlet mass flowrate to decrease, while the total mass flowrate (coolant plus mainstream) increased due to the lower temperature of the coolant (at fixed rotor capacity); (iv) at rotor inlet, the absolute and rotor-relative velocities decreased, causing the relative incidence angle to decrease and the relative total pressure to increase; (v) at rotor exit, the absolute total pressure increased as a result of the increased relative total pressure at rotor inlet; (vi) the HP stage reaction increased as a result of the change in operating point.

Experimental measurements and full 1.5-stage CFD simulations both supported the predictions of the mean-line model, in particular showing the key results of (i) increased HP vane-exit static pressure and (ii) increased absolute rotor-exit total pressure across the span (not only local to the cooled casing).

The CFD predictions showed an absolute stage efficiency benefit of 0.73% points for a coolant-to-mainstream mass flow ratio of 2.20%, which increased to 0.95% points for a coolant-to-mainstream mass flow ratio of 3.39%. The stage efficiency benefit was attributed to loss reduction in both the HP vane and rotor. The vane loss reduction was relatively small and was associated with reduced loading of the vane. The rotor loss reduction was almost an order of magnitude greater than that for the vane and was attributed in large part to the spoiling of the tip leakage flow, which resulted in a reduction in size and strength of the tip leakage vortex.

Single-row CFD simulations of the HP vane and rotor rows were run separately without cooling and with inflow and outflow boundary conditions imposed using radial profiles extracted from the cooled 1.5-stage simulation. These simulations were a contrivance, intended to offer a means of separating performance changes due to the *global* change in operating point (blade-row mismatching due to change in bulk-flow velocity triangles) and *local* changes such as tip leakage and secondary flow structure changes. Contributions from both global and local effects were positive, but the efficiency benefit associated with local effects was six times greater than that associated with the global effect. This is a key result, as, despite a number of previous studies in this area, the effects due to local and global changes have not previously been disambiguated. Indeed, the effect of global changes has largely been ignored in the literature.

It is noted that the efficiency benefit due to the global changes will typically be accounted for during preliminary 1D design and should therefore be achievable regardless of the cooling scheme. However, we argue that the benefit must also be accounted for during back-to-back assessments with respect to the uncooled (baseline) situation, whether experimental or computational; otherwise, the *overall* benefit may be under- or overestimated. Furthermore, it is important to understand how the introduction of coolant flows affects the turbine operating point if retrofitting to an existing design.

The results of this paper demonstrate the general sensitivity of the stage operating point to coolant introduction. In this study, blade-row mismatching effects (global effects) were observed to be significant in magnitude but to have only a small impact on stage efficiency in comparison to local effects (tip leakage flow changes and mixing). This may not hold true for other turbine designs, however, and we feel it is prudent to go some way to separate the two effects when analyzing designs. A further reason for this is that whilst blade-row mismatching effects did not significantly alter the power output for the particular 1.5-stage design (and associated boundary conditions) considered, there is no guarantee this result would hold for other turbine stages. The impact of effusion cooling on local flow changes, stage operating point changes, and power output should be considered holistically at an early stage in the design process.

Our conclusions, and the associated considerations for turbine stage analysis, are important for performance analysis of rotor-casing effusion cooling systems (the focus of this study) but are equally applicable for any cooling systems that cause mass introduction midway through the machine.

Acknowledgment

The financial support provided by Rolls-Royce plc is gratefully acknowledged. The authors would like to thank D. Cardwell and S. Chana of the University of Oxford for their assistance in running the experimental facility.

Nomenclature

a	= acoustic velocity, m s ⁻¹
h	= specific enthalpy, J kg ⁻¹
p	= pressure, bar
t	= time, s
v	= absolute velocity, m s ⁻¹
x	= axial position, m
M	= Mach number
N	= turbine rotational speed, rpm
R	= specific gas constant for dry air, J kg ⁻¹ K ⁻¹
S	= entropy, J K ⁻¹
T	= temperature, K
U	= rotor blade speed, m s ⁻¹
Y	= total pressure loss coefficient
\dot{m}	= mass flowrate, kg s ⁻¹

- \dot{w} = specific power, W kg⁻¹
 \dot{w} = power, W
 x_ϕ = axial position where 50% rotor turning is achieved, m
 A_{eff} = effective area, m²
 C_{ax} = vane or blade axial chord at 50% span, m
 C_d = discharge coefficient
 C_{visc} = viscous dissipation coefficient, $(T\dot{S}_{v,visc})/(\rho_3 v_{3,rel}^3/C_{ax})$
 M_{is} = isentropic Mach number
 C_{ax}^{tip} = rotor blade axial chord at tip, m
 Re_{HPV} = Reynolds number based on HP vane axial chord
 $\dot{S}_{v,visc}$ = rate of entropy creation per unit volume due to viscous dissipation

Greek Symbols

- α = yaw angle, deg
 β = pitch angle, deg
 γ = ratio of specific heat capacities
 Γ = capacity, kg s⁻¹ K^{1/2} Pa⁻¹, $\dot{m}\sqrt{T_0}/p_0$
 $\eta, \Delta\eta$ = efficiency, efficiency loss
 θ = tangential component
 Λ = HP stage reaction, $(h_2 - h_3)/(h_1 - h_3) \approx (p_2 - p_3)/(p_1 - p_3)$
 ξ = energy loss coefficient
 ρ = density, kg m⁻³
 ϕ = fraction of coolant mass injected upstream of x_ϕ in mean-line model, \dot{m}_{c2}/\dot{m}_c

Subscripts

- 0 = gas stagnation condition
 1 = turbine inlet
 2 = HP vane exit
 2a = HP vane exit, before coolant-mainstream mixing
 2b = HP vane exit, after coolant-mainstream mixing
 3 = HP rotor exit
 3a = HP rotor exit, before coolant-mainstream mixing
 3b = HP rotor exit, after coolant-mainstream mixing
 4 = IP vane exit
 c = coolant
 irr = irreversible
 m = coolant supply manifold
 N = nominal
 rel = relative frame
 w = wall
 x = axial component

Appendix: Mean-Line Model Description

First, conservation of mass is considered for the 1.5-stage turbine using the mass flowrate equations for each blade row

$$\dot{m}_1 = \frac{p_{01}}{\sqrt{T_{01}}} \Gamma_1 \left(\frac{p_2}{p_{01}} \right) \quad (A1)$$

$$\dot{m}_1 + \phi \dot{m}_c = \frac{p_{02,rel}}{\sqrt{T_{02,rel}}} \Gamma_2 \left(\frac{p_3}{p_{02,rel}} \right) \quad (A2)$$

$$\dot{m}_1 + \dot{m}_c = \frac{p_{03}}{\sqrt{T_{03}}} \Gamma_3 \left(\frac{p_4}{p_{03}} \right) \quad (A3)$$

The capacity characteristics used in the calculation for each blade row, Γ_i ($i = 1, 2, 3$), are numerically predicted trends shifted to match the experimentally measured stage mass flowrate values at the measured blade row pressure ratio. These capacity characteristics are assumed fixed throughout the mean-line analysis, although in reality, this may not be the case: analytical and 2D CFD predictions have indicated that HP vane film cooling causes a small reduction (of order 0.1%) in HP vane capacity [23].

The turbine-inlet boundary conditions, p_{01} and T_{01} , and IP vane-exit boundary condition, p_4 , are provided as inputs to the model. Equations (A1)–(A3) are solved simultaneously via iteration for the three independent variables, \dot{m}_1 , p_2 , and p_3 . At each iteration, the velocity triangles are calculated using the independent variables and the fixed parameters (listed in Table 6) as follows.

The angles α_2 and $\alpha_{3,rel}$ are assumed constant at the mass-mean values predicted by URANS calculations without cooling. This assumption is reasonable since the change in exit yaw angle due to off-design incidence angle is typically small for the ranges considered here [24]. The mid-span rotor blade speed, U , and specific gas constant, R , are also assumed fixed at the values listed in Table 6. All blade rows are assumed adiabatic.

At HP vane exit, $T_{02} = T_{01}$ by the adiabatic assumption, allowing M_2 to be calculated using

$$M_2 = \left[\frac{2}{\gamma - 1} \left(\frac{T_{02}}{T_2} - 1 \right) \right]^{1/2} \quad (A4)$$

and T_2 using

$$T_2 = T_{02} \left(\frac{p_2}{p_{02}} \right)^{(\gamma-1)/\gamma} \quad (A5)$$

The calculation of the HP vane-exit total pressure, p_{02} , accounts for a profile, secondary, and TE-thickness losses using the mean-line loss prediction method of Kacker and Okapuu [7]. The method estimates total pressure loss coefficients, which depend on details of the vane geometry and the vane-exit yaw angle, α_2 , and Mach number, M_2 . Since M_2 depends on T_2 via Eq. (A4), which in turn depends on p_{02} via Eq. (A5), the calculation of $p_{02} = p_{01} - Y_{vane}(\gamma/2)p_2 M_2^2$ must also be performed by iteration simultaneously with the calculation of M_2 .

Once M_2 and T_2 are determined, the rotor-relative inlet yaw angle, $\alpha_{2,rel}$, and Mach number, $M_{2,rel}$, are calculated using velocity triangles:

$$\alpha_{2,rel} = \tan^{-1} \frac{w_{\theta 2}}{w_{x 2}} \quad (A6)$$

$$M_{2,rel} = \frac{w_2}{\sqrt{\gamma R T_2}} \quad (A7)$$

The rotor-relative inlet stagnation conditions are then calculated using

$$T_{02,rel} = T_2 + \frac{w_2^2}{2c_p(T_2)} \quad (A8)$$

$$p_{02,rel} = p_2 \left(\frac{T_{02,rel}}{T_2} \right)^{\gamma/(\gamma-1)} \quad (A9)$$

Table 6 Turbine boundary conditions and operating parameters input to the mean-line model

Parameter	Value
p_{01} , bar	8.5
T_{01} , K	475
p_4/p_{01}	0.28
U , m s ⁻¹	247
α_2 , deg	75.0
$\alpha_{3,rel}$, deg	-70.9
R , J kg ⁻¹ K ⁻¹	287
c_p , J kg ⁻¹ K ⁻¹	1005
γ	1.4

At HP rotor exit, $M_{3,rel}$ is first calculated via iteration simultaneously with the calculation of T_3 as follows. Based on a guessed value of $M_{3,rel}$, the previously calculated values of $M_{2,rel}$ and α_2 , rel , and details of the rotor geometry (including β_3), total pressure loss coefficients are calculated, again using the method proposed by Kacker and Okapuu [7]. Additional profile loss due to off-design incidence angle on the rotor is estimated using the correlation reported by Benner et al. [8]. For both the vane and rotor, total pressure loss coefficients, Y_p , Y_s , and Y_{TET} , are calculated, which correspond to profile, secondary, and TE thickness losses, respectively. For the rotor, an additional total pressure loss coefficient, Y_{TC} , is estimated to account for losses associated with the tip clearance. For each loss source, the vane and rotor total pressure loss coefficients are defined as

$$Y = \frac{p_{01} - p_{02}}{\frac{1}{2}\rho_2 v_2^2}, \quad \frac{p_{02,rel} - p_{03,rel}}{\frac{1}{2}\rho_3 w_3^2} \quad (A10)$$

The rotor total-to-static efficiency is calculated as

$$\eta_{rotor} = 1 - \sum \xi \quad (A11)$$

where ξ are energy loss coefficients calculated using the total pressure loss coefficients and the summation is taken over each loss source (Y_p , Y_s , Y_{TET} , and Y_{TC}). For the rotor, the energy loss coefficients are defined as

$$\xi = \frac{w_{3s}^2 - w_3^2}{w_{3s}^2} = Y \left[1 + \frac{\gamma - 1}{2} M_{3,rel}^2 \right]^{-\gamma/(\gamma-1)} \quad (A12)$$

Using the estimated rotor total-to-static efficiency, T_3 is calculated using

$$T_3 = T_{03,rel} - \eta_{rotor}(T_{02,rel} - T_{3s}) \quad (A13)$$

To conclude the calculation of flow quantities at rotor exit, the absolute-frame stagnation conditions are computed. This requires converting

$$p_{03,rel} = p_3 \left(1 + \frac{\gamma - 1}{2} M_{3,rel}^2 \right)^{\gamma/(\gamma-1)} \quad (A14)$$

from the relative frame into the absolute frame. Using velocity triangle relations analogous to Eqs. (A6) and (A7)

$$\alpha_3 = \tan^{-1} \frac{v_{\theta 3}}{v_{x3}} \quad (A15)$$

$$M_3 = \frac{v_3}{\sqrt{\gamma R T_3}} \quad (A16)$$

The absolute-frame stagnation conditions at rotor exit are then given by

$$T_{03} = T_3 + \frac{v_3^2}{2c_p(T_3)} \quad (A17)$$

$$p_{03} = p_3 \left(\frac{T_{03}}{T_3} \right)^{\gamma/(\gamma-1)} \quad (A18)$$

References

- [1] Chana, K. S., and Haller, B., 2009, "Novel Turbine Rotor Shroud Film-Cooling Design and Validation: Part 1," ASME Paper No. GT2009-60242.
- [2] Chana, K. S., and Haller, B., 2009, "Novel Turbine Rotor Shroud Film-Cooling Design and Validation: Part 2," ASME Paper No. GT2009-60246.
- [3] Collins, M., Chana, K., and Povey, T., 2017, "Application of Film Cooling to an Unshrouded High-Pressure Turbine Casing," *ASME J. Turbomach.*, **139**(6), p. 061010.
- [4] Collins, M., and Povey, T., 2015, "Exploitation of Acoustic Effects in Film Cooling," *ASME J. Eng. Gas Turbines Power*, **137**(10), p. 102602.
- [5] Mischo, B., Burdet, A., Behr, T., and Abhari, R. S., 2007, "Control of Rotor Tip Leakage Through Cooling Injection From Casing in a High-Work Turbine: Computational Investigation Using a Feature-Based jet Model," ASME Paper No. GT2007-27669.
- [6] Behr, T., Kalfas, A. I., and Abhari, R. S., 2008, "Control of Rotor Tip Leakage Through Cooling Injection From the Casing in a High-Work Turbine," *ASME J. Turbomach.*, **130**(3), p. 031014.
- [7] Kacker, S. C., and Okapuu, U., 1982, "A Mean Line Prediction Method for Axial Flow Turbine Efficiency," *J. Eng. Power*, **104**(1), pp. 111–119.
- [8] Benner, M. W., Sjolander, S. A., and Moustapha, S. H., 1997, "Influence of Leading-Edge Geometry on Profile Losses in Turbines at Off-Design Incidence: Experimental Results and an Improved Correlation," *ASME J. Turbomach.*, **119**(2), pp. 193–200.
- [9] Hartsel, J. E., 1972, "Prediction of Effects of Mass-Transfer Cooling on the Blade-Row Efficiency of Turbine Airfoils," Proceedings of the 10th AIAA Aerospace Sciences Meeting, San Diego, CA, Jan. 17–19, p. 11.
- [10] Hilditch, M. A., Fowler, A., Jones, T. V., Chana, K. S., Oldfield, M. L. G., Ainsworth, R. W., Hogg, S. I., Anderson, S. J., and Smith, G. C., 1994, "Installation of a Turbine Stage in the Pyestock Isentropic Light Piston Facility," ASME Paper No. 94-GT-277.
- [11] Beard, P. F., Adams, M. G., Stokes, M. R., Wallin, F., Cardwell, D. N., Povey, T., and Chana, K. S., 2019, "The LEMCOTEC 1½ Stage Film-Cooled HP Turbine: Design, Integration, and Testing in the Oxford Turbine Research Facility," Proceedings of the 13th European Conference on Turbomachinery Fluid Dynamics and Thermodynamics, Lausanne, Switzerland, Apr. 7–12 April.
- [12] Povey, T., Sharpe, M., and Rawlinson, A., 2011, "Experimental Measurements of Gas Turbine Flow Capacity Using a Novel Transient Technique," *ASME J. Turbomach.*, **133**(1), p. 011005.
- [13] Kirolos, B., and Povey, T., 2017, "Method for Accurately Evaluating Flow Capacity of Individual Film-Cooling Rows of Engine Components," *ASME J. Turbomach.*, **139**(11), p. 111004.
- [14] Bryer, D. W., and Pankhurst, R. C., 1971, *Pressure-Probe Methods for Determining Wind Speed and Flow Direction*, HMSO.
- [15] Hall, B. F., and Povey, T., 2017, "The Oxford Probe: An Open Access Five-Hole Probe for Aerodynamic Measurements," *Meas. Sci. Technol.*, **28**(3), p. 035004.
- [16] Hall, B. F., and Povey, T., 2018, "A Practical Model for Pressure Probe System Response Estimation (With Review of Existing Models)," *Meas. Sci. Technol.*, **29**(4), p. 045301.
- [17] Paniagua, G., Dénos, R., and Oropesa, M., 2002, "Thermocouple Probes for Accurate Temperature Measurements in Short Duration Facilities," ASME Paper No. GT2002-30043.
- [18] Lapworth, L., 2004, "Hydra-CFD: A Framework for Collaborative CFD Development," International Conference on Scientific and Engineering Computation (IC-SEC), Singapore, June 30–July 2.
- [19] Milli, A., and Shahpar, S., 2012, "PADRAM: Parametric Design and Rapid Meshing System for Complex Turbomachinery Configurations," ASME Paper No. GT2012-69030.
- [20] Yamamoto, A., 1988, "Interaction Mechanisms Between tip Leakage Flow and the Passage Vortex in a Linear Turbine Rotor Cascade," *ASME J. Turbomach.*, **110**(3), pp. 329–338.
- [21] Palafox, P., Oldfield, M. L. G., LaGraff, J. E., and Jones, T. V., 2008, "PIV Maps of tip Leakage and Secondary Flow Fields on a Low-Speed Turbine Blade Cascade With Moving End Wall," *ASME J. Turbomach.*, **130**(1), p. 011001.
- [22] Miller, R. J., 2013, "Mechanical Work Potential," ASME Paper No. GT2013-95488.
- [23] Hambidge, C., and Povey, T., 2012, "Numerical and Analytical Study of the Effect of Film Cooling on HP NGV Capacity," ASME Paper No. GT2012-69066.
- [24] Ainley, D. G., and Mathieson, G. C. R., 1951, "A Method of Performance Estimation for Axial-Flow Turbines," A.R.C. Technical Report R&M, No. 2974.